MODELLISTICA E CALCOLO SCIENTIFICO

MODELING AND SCIENTIFIC COMPUTING

MOX-Report No. 54/2021

HOW TO BEST CHOOSE THE OUTER COARSE MESH IN THE DOMAIN DECOMPOSITION METHOD OF BANK AND JIMACK

Ciaramella, G.; Gander, M.J.; Mamooler, P.

MOX, Dipartimento di Matematica
Politecnico di Milano, Via Bonardi 9 - 20133 Milano (Italy)

mox-dmat@polimi.it http://mox.polimi.it

HOW TO BEST CHOOSE THE OUTER COARSE MESH IN THE DOMAIN DECOMPOSITION METHOD OF BANK AND JIMACK

G. CIARAMELLA*, M.J. GANDER †, AND P. MAMOOLER ‡

Abstract. In [7] we defined a new partition of unity for the Bank-Jimack domain decomposition method in 1D and proved that with the new partition of unity, the Bank-Jimack method is an optimal Schwarz method in 1D and thus converges in two iterations for two subdomains: it becomes a direct solver, and this independently of the outer coarse mesh one uses! In this paper, we show that the Bank-Jimack method in 2D is an optimized Schwarz method and its convergence behavior depends on the structure of the outer coarse mesh each subdomain is using. For an equally spaced coarse mesh its convergence behavior is not as good as the convergence behavior of optimized Schwarz. However, if a stretched coarse mesh is used, then the Bank-Jimack method becomes faster then optimized Schwarz with Robin or Ventcell transmission conditions. Our analysis leads to a conjecture stating that the convergence factor of the Bank-Jimack method with overlap L and m geometrically stretched outer coarse mesh cells is $1 - O(L^{\frac{1}{2m}})$.

Key words. Optimized Schwarz method, Bank-Jimack method, domain decomposition methods, Poisson equation.

1. Introduction.

In 2001 Randolph E. Bank and Peter K. Jimack [1] introduced a new domain decomposition method for the adaptive solution of elliptic partial differential equations, see also [2] for a convergence analysis in the context of the abstract Schwarz framework, and [25] and references therein for an introduction to such techniques. The novel feature of the Bank-Jimack method (BJM) is that each of the subproblems is defined over the entire domain, but outside of the subdomain, a coarse mesh is used. The method is formulated as a residual correction method, and it is not easy to interpret how and what information is transmitted between subdomains through the outer coarse mesh each subdomain has. A similar difficulty of interpretation existed as well for Additive Schwarz and Restricted Additive Schwarz [8, 22, 12]. This is very different compared to classical domain decomposition methods where this is well understood: classical Schwarz methods [21] exchange information through Dirichlet transmission conditions and use overlap, FETI [10, 9] and Neumann-Neumann methods [3, 19, 20] use Dirichlet and Neumann conditions without overlap, and optimized Schwarz methods (OSMs), which go back to Lions, [17] use Robin or higher order transmission conditions and work with or without overlap, see [11, 12] for an introduction and historic perspective of OSMs. In [7], we showed for a one-dimensional Poisson problem and two subdomains that if one introduces a more general partition of unity, then the BJM becomes an optimal Schwarz method, i.e. a direct solver for the problem converging in two iterations, and this independently of how coarse the outer mesh is. The BJM thus faithfully constructs a Robin type transmission condition involving the Dirichlet to Neumann map in 1D. We analyze here the BJM for the Poisson equation in 2 dimension and two subdomains, and show that with the modified partition of unity, the method can be interpreted as an OSM. Its convergence now depends on the structure of the outer coarse mesh each subdomain uses. In case of equally spaced coarse meshes, we prove that the asymptotic convergence factor is not as good as for an OSM. If one uses however a stretched coarse mesh, i.e. a mesh which becomes gradually more and more coarse in a specific way as one gets further away from the subdomain boundary, the method converges faster than the classical zeroth and second-order OSMs. Based on extensive numerical and asymptotic studies of

*Politecnico di Milano, Dipartimento di Matematica, MOX Lab (gabriele.ciaramella@polimi.it).
†Université de Genève, Section de mathématiques (martin.gander@unige.ch).
‡Université de Genève, Section de mathématiques (parisa.mamooler@unige.ch).

the analytical convergence factor and the position of coarse points, we conjecture an asymptotic formula for the contraction factor of the BJM. Our analysis also indicates a close relation of the BJM to the class of sweeping type preconditioners [16], since the outer coarse mesh can be interpreted as an implementation of a PML transmission condition, but the BJM is not restricted to sequential decompositions without cross points.

Our paper is organized as follows: in Section 2, the BJM is recalled for a general PDE problem and its generalization by a partition of unity function is introduced (for the influence of partitions of unity on overlapping domain decomposition methods, see [13]). Moreover, for the Laplace problem in two dimensions the BJM is described in detail. The convergence analysis of the BJM is carried out in Section 3, where it is proved to be equivalent to an OSM. This important relation allows us to obtain sharp convergence results. Section 4 is devoted to extensive numerical experiments leading to our conjecture. Finally, our conclusions are presented in Section 5.

2. The Bank-Jimack domain decomposition method.

In this section, we give a precise description of the BJM, and introduce our model problem and the Fourier techniques that we will use.

2.1. Description of the method.

Let us consider a general self-adjoint[1] linear elliptic PDE $\mathcal{L}u = f$ in a domain Ω with homogeneous Dirichlet boundary conditions on $\partial\Omega$. Discretizing the problem on a global fine mesh leads to a linear system $A\boldsymbol{u} = \boldsymbol{f}$, where the matrix A is the discrete counterpart of $\mathcal{L}$, $\boldsymbol{u}$ is the vector of unknown nodal values on the global fine mesh, and $\boldsymbol{f}$ is the load vector.

To describe the BJM, we decompose Ω into two overlapping subdomains, $\Omega = \Omega_1 \cup \Omega_2$. The unknown vector $\boldsymbol{u}$ is partitioned accordingly as $\boldsymbol{u} = \left[\boldsymbol{u}_1^\top, \boldsymbol{u}_s^\top, \boldsymbol{u}_2^\top\right]^\top$, where $\boldsymbol{u}_1$ is the vector of unknowns on the nodes in $\Omega_1 \setminus \Omega_2$, $\boldsymbol{u}_s$ is the vector of unknowns on the nodes in the overlap $\Omega_1 \cap \Omega_2$, and $\boldsymbol{u}_2$ is the vector of unknowns on the nodes in $\Omega_2 \setminus \Omega_1$. We can then write the linear system $A\boldsymbol{u} = \boldsymbol{f}$ in block-matrix form,

$$\begin{bmatrix} A_1 & B_1 & 0 \\ B_1^\top & A_s & B_2^\top \\ 0 & B_2 & A_2 \end{bmatrix} \begin{bmatrix} \boldsymbol{u}_1 \\ \boldsymbol{u}_s \\ \boldsymbol{u}_2 \end{bmatrix} = \begin{bmatrix} \boldsymbol{f}_1 \\ \boldsymbol{f}_s \\ \boldsymbol{f}_2 \end{bmatrix}. \tag{2.1}$$

The idea of the BJM is to consider two further meshes on Ω, one identical to the original fine mesh in Ω_1, but coarse on $\Omega \setminus \Omega_1$, and one identical to the original fine mesh in Ω_2, but coarse on $\Omega \setminus \Omega_2$. This leads to the two further linear systems

$$A_{\Omega_1}\boldsymbol{v} = T_2\boldsymbol{f} \quad \text{and} \quad A_{\Omega_2}\boldsymbol{w} = T_1\boldsymbol{f}, \tag{2.2}$$

with

$$\begin{aligned} A_{\Omega_1} &:= \begin{bmatrix} A_1 & B_1 & 0 \\ B_1^\top & A_s & C_2 \\ 0 & \widetilde{B}_2 & \widetilde{A}_2 \end{bmatrix}, \quad \boldsymbol{v} := \begin{bmatrix} \boldsymbol{v}_1 \\ \boldsymbol{v}_s \\ \boldsymbol{v}_2 \end{bmatrix}, \quad T_2 := \begin{bmatrix} I_1 & \\ & M_2 \end{bmatrix}, \\ A_{\Omega_2} &:= \begin{bmatrix} \widetilde{A}_1 & \widetilde{B}_1 & 0 \\ C_1 & A_s & B_2^\top \\ 0 & B_2 & A_2 \end{bmatrix}, \quad \boldsymbol{w} := \begin{bmatrix} \boldsymbol{w}_1 \\ \boldsymbol{w}_s \\ \boldsymbol{w}_2 \end{bmatrix}, \quad T_1 := \begin{bmatrix} M_1 & \\ & I_2 \end{bmatrix}, \end{aligned} \tag{2.3}$$

[1] BJM is also defined for non-self-adjoint problems. We assume this here only to simplify the notation.

Algorithm 2.1 Bank-Jimack Domain Decomposition Method:

1: Set $k = 0$ and choose an initial guess $\boldsymbol{u}^0$.
2: Repeat until convergence

2.1 $$\begin{bmatrix}\boldsymbol{r}_1^k\\ \boldsymbol{r}_s^k\\ \boldsymbol{r}_2^k\end{bmatrix} := \begin{bmatrix}\boldsymbol{f}_1\\ \boldsymbol{f}_s\\ \boldsymbol{f}_2\end{bmatrix} - \begin{bmatrix}A_1 & B_1 & 0\\ B_1^\top & A_s & B_2^\top\\ 0 & B_2 & A_2\end{bmatrix}\begin{bmatrix}\boldsymbol{u}_1^k\\ \boldsymbol{u}_s^k\\ \boldsymbol{u}_2^k\end{bmatrix}$$

2.2 Solve $A_{\Omega_1}\boldsymbol{v}^k = T_2\boldsymbol{r}^k$ and $A_{\Omega_2}\boldsymbol{w}^k = T_1\boldsymbol{r}^k$, that are explicitly written as

$$\begin{bmatrix}A_1 & B_1 & 0\\ B_1^\top & A_s & C_2\\ 0 & \widetilde{B}_2 & \widetilde{A}_2\end{bmatrix}\begin{bmatrix}\boldsymbol{v}_1^k\\ \boldsymbol{v}_s^k\\ \boldsymbol{v}_2^k\end{bmatrix} = \begin{bmatrix}\boldsymbol{r}_1^k\\ \boldsymbol{r}_s^k\\ M_2\boldsymbol{r}_2^k\end{bmatrix}, \quad \begin{bmatrix}\widetilde{A}_1 & \widetilde{B}_1 & 0\\ C_1 & A_s & B_2^\top\\ 0 & B_2 & A_2\end{bmatrix}\begin{bmatrix}\boldsymbol{w}_1^k\\ \boldsymbol{w}_s^k\\ \boldsymbol{w}_2^k\end{bmatrix} = \begin{bmatrix}M_1\boldsymbol{r}_1^k\\ \boldsymbol{r}_s^k\\ \boldsymbol{r}_2^k\end{bmatrix}$$

2.3 $$\begin{bmatrix}\boldsymbol{u}_1^{k+1}\\ \boldsymbol{u}_s^{k+1}\\ \boldsymbol{u}_2^{k+1}\end{bmatrix} := \begin{bmatrix}\boldsymbol{u}_1^k\\ \boldsymbol{u}_s^k\\ \boldsymbol{u}_2^k\end{bmatrix} + \begin{bmatrix}\boldsymbol{v}_1^k\\ \frac{1}{2}(\boldsymbol{v}_s^k + \boldsymbol{w}_s^k)\\ \boldsymbol{w}_2^k\end{bmatrix}$$

2.4 $k := k+1$

where we introduced the restriction matrices M_j, $j = 1, 2$, to map the fine-mesh vectors $\boldsymbol{f}_j$ to the corresponding coarse meshes, and I_1 and I_2 are identities of appropriate sizes. Notice that, depending on the chosen discretization scheme, one could get $C_1 = \widetilde{B}_1^\top$ and $C_2 = \widetilde{B}_2^\top$, which leads to symmetric matrices A_{Ω_1} and A_{Ω_2}. However, this symmetry is not generally guaranteed, as we are going to see in the next sections. The BJM as a stationary iteration is then described by Algorithm 2.1.

In [7] we studied the BJM for a one-dimensional problem and showed that, in general, it does not lead to a convergent stationary iteration. To correct this behavior we introduced a discrete partition of unity $D_1 + D_2 = I$, where I is the identity matrix and D_1 and D_2 are two matrices that for a one-dimensional problem must have the form ($\times$ denote arbitrary entries satisfying the sum condition)

$$D_1 = \operatorname{diag}(1, \times, \ldots, \times, 0) \quad \text{and} \quad D_2 = \operatorname{diag}(0, \times, \ldots, \times, 1). \tag{2.4}$$

Using these matrices, we modified the BJM by replacing Step 2.3 in Algorithm 2.1 with

$$\begin{bmatrix}\boldsymbol{u}_1^{k+1}\\ \boldsymbol{u}_s^{k+1}\\ \boldsymbol{u}_2^{k+1}\end{bmatrix} := \begin{bmatrix}\boldsymbol{u}_1^k\\ \boldsymbol{u}_s^k\\ \boldsymbol{u}_2^k\end{bmatrix} + \begin{bmatrix}\boldsymbol{v}_1^k\\ D_1\boldsymbol{v}_s^k + D_2\boldsymbol{w}_s^k\\ \boldsymbol{w}_2^k\end{bmatrix}. \tag{2.5}$$

This leads to an iterative method that we proved to be convergent and equivalent to an optimal Schwarz method [15] for the one-dimensional Poisson problem [7]. In [7] we also showed, by direct numerical experiments, that this equivalence does not hold for the two-dimensional Poisson problem. Our goal here is to analyze the convergence of the BJM for two-dimensional problems. Notice that, in what follows, we always refer to BJM as the method obtained by using (2.5) in Algorithm 2.1.

2.2. The BJM for the Poisson Equation in 2D. Let us consider the problem

$$\begin{aligned} -\Delta u &= f \quad \text{in} \quad \Omega = (0,1)\times(0,1),\\ u &= 0 \quad \text{on} \quad \partial\Omega, \end{aligned} \tag{2.6}$$

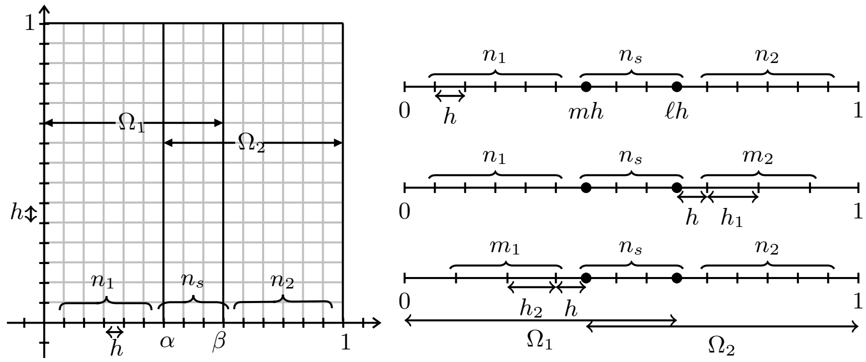

(a) (b)

Fig. 2.1: (a) A global fine mesh on $\Omega = (0,1) \times (0,1)$ and the decomposition $\Omega = \Omega_1 \cup \Omega_2$. (b) Global fine mesh in direction x (top row), and two partially coarse meshes corresponding to the left subdomain Ω_1 (middle row) and to the right subdomain Ω_2 (bottom row). The black dots represent the x-coordinates of the interfaces, namely mh and ℓh.

where Δ is the Laplace operator and f is a sufficiently regular right-hand side function. We consider a uniform grid in $\Omega = (0,1) \times (0,1)$ of N interior points in each direction and mesh size $h := \frac{1}{N+1}$; see, e.g., Figure 2.1 (a). We then discretize (2.6) by a second-order finite-difference scheme, which leads to a linear system $A\boldsymbol{u} = \boldsymbol{f}$, where $A \in \mathbb{R}^{N^2 \times N^2}$ is the classical (pentadiagonal) discrete Laplace operator. This system can be easily partitioned as in (2.1). We assume that the vector of unknowns $\boldsymbol{u}$ is obtained as $\boldsymbol{u} = [\boldsymbol{u}_1^\top, \dots, \boldsymbol{u}_N^\top]^\top$, where $\boldsymbol{u}_j \in \mathbb{R}^N$ contains the unknown values on the jth column of the grid. In this case, the matrix A can be expressed in the Kronecker format $A = I_y \otimes A_x + A_y \otimes I_x$, where A_x and A_y are $N \times N$ one-dimensional discrete Laplace matrices in directions x and y, and I_x and I_y are $N \times N$ identity matrices.

The BJM requires two partially-coarse grids. We assume that, in direction x our decomposition $\Omega = \Omega_1 \cup \Omega_2$ has n_1 interior points $\Omega_1 \setminus \Omega_2$, n_2 interior points in $\Omega_2 \setminus \Omega_1$, and n_s points in $\Omega_1 \cap \Omega_2$; see Figure 2.1 (a). For our analysis, the coarsening is performed only in x-direction[2], as shown in Figure 2.1 (b), while the grid in direction y is maintained fine. The partially coarse-grids have m_2 coarse points in $\Omega_2 \setminus \Omega_1$ (Figure 2.1 (b), middle row) and m_1 coarse points in $\Omega_1 \setminus \Omega_2$ (Figure 2.1 (b), bottom row) and the corresponding mesh sizes are h_1 and h_2[3]. If we denote by $A_{x,1}$ and $A_{x,2}$ the one-dimensional finite-difference Laplace matrices in x-direction, then the partially-coarse matrices A_{Ω_1} and A_{Ω_2} are

$$A_{\Omega_1} = I_y \otimes A_{x,1} + A_y \otimes I_{x,1} \text{ and } A_{\Omega_2} = I_y \otimes A_{x,2} + A_y \otimes I_{x,2}, \tag{2.7}$$

where $I_{x,1}$ and $I_{x,2}$ are identities of sizes $n_1 + n_s + m_2$ and $m_1 + n_s + n_2$, respectively. Notice that, the matrices $A_{x,1}$ and $A_{x,2}$ are classical second-order finite difference matrices in 1D, defined on the

[2]In our numerical experiments, we will test also coarsening in both directions.

[3]Notice that the first coarse points, namely the point number $n_1 + n_2 + 1$ for the first mesh and the point number m_1 for the second mesh, are located at distance h from the interfaces. This choice is motivated by the fact that we will define discrete (finite-difference) derivatives across these points and then in Section 3 take limits for $h \to 0$, while keeping the numbers m_1 and m_2 of coarse points fixed.

union of two uniform grids. Therefore, the only entries that differ from a standard finite-difference formula are the ones corresponding to the stencil across the mesh changes. For example, the five-point formulas for $A_{x,1}$ on fine and coarse meshes are $(A_{x,1}v)_j = \frac{-v_{j-1}+2v_j-v_{j+1}}{h^2}$, for $j \leq n_1+n_2$, and $(A_{x,1}\boldsymbol{v})_j = \frac{-v_{j-1}+2v_j-v_{j+1}}{h_1^2}$, for $j \geq n_1+n_2+2$, while at the point across the mesh change (see also Figure 2.1), we have

$$(A_{x,1}v)_j = -\frac{2v_{j-1}}{h(h+h_1)} + \frac{2v_j}{hh_1} - \frac{2v_{j+1}}{h_1(h+h_1)}, \text{ for } j = n_1+n_s+1.$$

The matrices A_{Ω_1} and A_{Ω_2} can be partitioned exactly as in (2.3), and the restriction matrices T_1 and T_2 have now the forms

$$T_1 = I_y \otimes \begin{bmatrix} I_{n_1+n_s} & 0 \\ 0 & \widehat{M}_2 \end{bmatrix} \text{ and } T_2 = I_y \otimes \begin{bmatrix} \widehat{M}_1 & 0 \\ 0 & I_{n_s+n_2} \end{bmatrix}, \tag{2.8}$$

where $\widehat{M}_1 \in \mathbb{R}^{m_1 \times n_1}$ and $\widehat{M}_2 \in \mathbb{R}^{m_2 \times n_2}$ are one-dimensional restriction matrices and $I_{n_s+n_2}$ and $I_{n_1+n_s}$ are identity matrices of sizes n_s+n_2 and n_1+n_s. It remains to describe the matrices $D_1 \in \mathbb{R}^{Nn_s \times Nn_s}$ and $D_2 \in \mathbb{R}^{Nn_s \times Nn_s}$ used in (2.5). These form a partition of unity, that is $D_1 + D_2 = I_{Nn_s}$, where I_{Nn_s} is an identity of size Nn_s, and have the forms

$$\begin{aligned} D_1 &= I_y \otimes \widehat{D}_1, \text{ with } \widehat{D}_1 = \mathrm{diag}(1, \times, \dots, \times, 0) \in \mathbb{R}^{n_s}, \\ D_2 &= I_y \otimes \widehat{D}_2, \text{ with } \widehat{D}_2 = \mathrm{diag}(0, \times, \dots, \times, 1) \in \mathbb{R}^{n_s}. \end{aligned} \tag{2.9}$$

We have then described all the components that allow us to use the BJM (namely Algorithm 2.1) for the two-dimensional Poisson problem (2.6).

The choice of discretization by the finite-difference method allows us to perform a detailed convergence analysis based on the diagonalization obtained in Section 2.3.

2.3. A discrete Fourier expansion and the $\eta - \Delta$ equation in 1D. The finite-difference matrices A, A_{Ω_1} and A_{Ω_2} have similar structures based on Kronecker-product expansions: the matrix components in direction y are the same and are not coarsened. Hence, the one-dimensional discrete Laplace matrix A_y appears unchanged in A, A_{Ω_1} and A_{Ω_2}, while the matrix A_x appearing in A is replaced in A_{Ω_1} by $A_{x,1}$ and in A_{Ω_2} by $A_{x,2}$.

It is important to notice that A_y is a tridiagonal Toeplitz matrix having values $2/h^2$ on the main diagonal and values $-1/h^2$ on the first upper and lower diagonals. It is well-known that A_y can be diagonalized as $U^\top A_y U = \Lambda$, where $\Lambda = \mathrm{diag}(\lambda_1, \dots, \lambda_N)$ with $\lambda_j > 0$, and the columns of the orthogonal matrix $U \in \mathbb{R}^{N \times N}$ are normalized discrete Fourier sine modes. If one now defines $\widehat{U} := U \otimes I_x$, then it is possible to block-diagonalize A,

$$\widehat{U}^\top A \widehat{U} = I_y \otimes A_x + \Lambda \otimes I_x = \begin{bmatrix} A_x + \lambda_1 I_x & & \\ & \ddots & \\ & & A_x + \lambda_N I_x \end{bmatrix}, \tag{2.10}$$

where we used the property $(C_1 \otimes C_2)(C_3 \otimes C_4) = (C_1C_3) \otimes (C_2C_4)$, for any matrices C_1, C_2, C_3, and C_4 such that the matrix products C_1C_3 and C_2C_4 can be formed. Defining the vectors $\widehat{\boldsymbol{u}} := \widehat{U}^\top \boldsymbol{u}$ and $\widehat{\boldsymbol{f}} := \widehat{U}^\top \boldsymbol{f}$ and decomposing them as $\widehat{\boldsymbol{u}} = [\widehat{\boldsymbol{u}}_1^\top, \dots, \widehat{\boldsymbol{u}}_N^\top]^\top$ and $\widehat{\boldsymbol{f}} = [\widehat{\boldsymbol{f}}_1^\top, \dots, \widehat{\boldsymbol{f}}_N^\top]^\top$, we obtain that the linear system $A\boldsymbol{u} = \boldsymbol{f}$ can be equivalently written as

$$(A_x + \lambda_j I_x)\widehat{\boldsymbol{u}}_j = \widehat{\boldsymbol{f}}_j \text{ for } j = 1, \dots, N. \tag{2.11}$$

This is the discrete version of a Fourier sine diagonalization of the continuous problem (2.6); see, e.g, [5]. Notice that each component $\widehat{\boldsymbol{u}}_j \in \mathbb{R}^N$ still represents a vector of nodal values on the jth row of the discretization grid. Hence, we can decompose it as $\widehat{\boldsymbol{u}}_j = [\widehat{\boldsymbol{u}}_{j,1}^\top, \widehat{\boldsymbol{u}}_{j,s}^\top, \widehat{\boldsymbol{u}}_{j,2}^\top]^\top$, where $\widehat{\boldsymbol{u}}_{j,1} \in \mathbb{R}^{n_1}$ has values on the nodes in $\Omega_1 \setminus \Omega_2$, $\widehat{\boldsymbol{u}}_{j,2} \in \mathbb{R}^{n_2}$ has values on the nodes in $\Omega_2 \setminus \Omega_1$, and $\widehat{\boldsymbol{u}}_{j,s} \in \mathbb{R}^{n_s}$ has values on the nodes in $\Omega_1 \cap \Omega_2$.

Now, using the block-diagonalized form (2.10)-(2.11), we will rewrite the BJM algorithm for each component j of $\widehat{\boldsymbol{u}}$. Given an approximation $\boldsymbol{u}^k$ obtained at the kth iteration of Algorithm 2.1, one can compute $\widehat{\boldsymbol{u}}^k = U^\top \boldsymbol{u}^k$ and $\widehat{\boldsymbol{r}}^k = U^\top \boldsymbol{r}^k$ and rewrite Step 2.1 as

$$\widehat{\boldsymbol{r}}_j^k = \widehat{\boldsymbol{f}}_j - (A_x + \lambda_j I_x)\widehat{\boldsymbol{u}}_j^k \text{ for } j = 1, \dots, N. \tag{2.12}$$

Similarly as for the system $A\boldsymbol{u} = \boldsymbol{f}$, we can transform the residual subsystems of Step 2.2. To do so, we define $\widehat{U}_i := U \otimes I_{x,i}$, for $i = 1, 2$, such that $\widehat{\boldsymbol{v}}^k = \widehat{U}_1^\top \boldsymbol{v}^k$ and $\widehat{\boldsymbol{w}}^k = \widehat{U}_2^\top \boldsymbol{w}^k$, and write the subsystems $A_{\Omega_1}\boldsymbol{v}^k = T_2 \boldsymbol{r}^k$ and $A_{\Omega_2}\boldsymbol{w}^k = T_1 \boldsymbol{r}^k$ as

$$\widehat{U}_1^\top A_{\Omega_1} \widehat{U}_1 \widehat{U}_1^\top \boldsymbol{v}^k = \widehat{U}_1^\top T_2 \widehat{U} \widehat{U}^\top \boldsymbol{r}^k \quad \text{and} \quad \widehat{U}_2^\top A_{\Omega_2} \widehat{U}_2 \widehat{U}_2^\top \boldsymbol{w}^k = \widehat{U}_2^\top T_1 \widehat{U} \widehat{U}^\top \boldsymbol{r}^k,$$

which allows us to obtain

$$\widehat{U}_1^\top A_{\Omega_1} \widehat{U}_1 \widehat{\boldsymbol{v}}^k = \widehat{U}_1^\top T_2 \widehat{U} \widehat{\boldsymbol{r}}^k \quad \text{and} \quad \widehat{U}_2^\top A_{\Omega_2} \widehat{U}_2 \widehat{\boldsymbol{w}}^k = \widehat{U}_2^\top T_1 \widehat{U} \widehat{\boldsymbol{r}}^k. \tag{2.13}$$

Now, using the structures of A_{Ω_i} given in (2.7), we obtain

$$\widehat{U}_i^\top A_{\Omega_i} \widehat{U}_i = I_y \otimes A_{x,i} + \Lambda \otimes I_{x,i} = \begin{bmatrix} A_{x,i} + \lambda_1 I_{x,i} & & \\ & \ddots & \\ & & A_{x,i} + \lambda_N I_{x,i} \end{bmatrix}, \tag{2.14}$$

for $i = 1, 2$, and recalling the matrices T_i, defined in (2.8), we get

$$\widehat{U}_1^\top T_1 \widehat{U} = (U^\top \otimes I_{x,1})(I_y \otimes \begin{bmatrix} I_{n_1+n_s} & 0 \\ 0 & \widehat{M}_2 \end{bmatrix})(U \otimes I_x) = I_y \otimes \begin{bmatrix} I_{n_1+n_s} & 0 \\ 0 & \widehat{M}_2 \end{bmatrix} \tag{2.15}$$

and

$$\widehat{U}_2^\top T_2 \widehat{U} = (U^\top \otimes I_{x,2})(I_y \otimes \begin{bmatrix} \widehat{M}_1 & 0 \\ 0 & I_{n_2+n_s} \end{bmatrix})(U \otimes I_x) = I_y \otimes \begin{bmatrix} \widehat{M}_1 & 0 \\ 0 & I_{n_2+n_s} \end{bmatrix}. \tag{2.16}$$

Replacing (2.14), (2.15) and (2.16) into (2.13), we rewrite the residual systems in Step 2.2 as

$$\begin{aligned} (A_{x,1} + \lambda_j I_{x,1})\widehat{\boldsymbol{v}}_j^k &= \begin{bmatrix} I_{n_1+n_s} & 0 \\ 0 & \widehat{M}_2 \end{bmatrix} \widehat{\boldsymbol{r}}_j^k, \\ (A_{x,2} + \lambda_j I_{x,2})\widehat{\boldsymbol{w}}_j^k &= \begin{bmatrix} \widehat{M}_1 & 0 \\ 0 & I_{n_2+n_s} \end{bmatrix} \widehat{\boldsymbol{r}}_j^k, \end{aligned} \tag{2.17}$$

for $j = 1, \dots, N$. It remains to study equation (2.5) (with the matrices D_i defined in (2.9)) that represents Step 2.3. This equation can be written in the compact form

$$\boldsymbol{u}^{k+1} = \boldsymbol{u}^k + (I_y \otimes D_1^e)\boldsymbol{v}^k + (I_y \otimes D_2^e)\boldsymbol{w}^k, \tag{2.18}$$

where $D_1^e \in \mathbb{R}^{N\times(n_1+n_s+m_2)}$ and $D_2^e \in \mathbb{R}^{N\times(m_1+n_s+n_2)}$ are given by

$$D_1^e = \begin{bmatrix} I_{n_1} & & \\ & \widehat{D}_1 & \\ & & 0 \end{bmatrix} \text{ and } D_2^e = \begin{bmatrix} 0 & & \\ & \widehat{D}_2 & \\ & & I_{n_2} \end{bmatrix}.$$

Now, using (2.18) we get

$$\widehat{U}^\top \boldsymbol{u}^{k+1} = \widehat{U}^\top \boldsymbol{u}^k + \widehat{U}^\top (I_y \otimes D_1^e)\widehat{U}_1\widehat{U}_1^\top \boldsymbol{v}^k + \widehat{U}^\top (I_y \otimes D_2^e)\widehat{U}_2\widehat{U}_2^\top \boldsymbol{w}^k,$$

and recalling the structures of D_1^e and D_2^e, we obtain

$$\begin{bmatrix} \widehat{\boldsymbol{u}}_{j,1}^{k+1} \\ \widehat{\boldsymbol{u}}_{j,s}^{k+1} \\ \widehat{\boldsymbol{u}}_{j,2}^{k+1} \end{bmatrix} = \begin{bmatrix} \widehat{\boldsymbol{u}}_{j,1}^{k} \\ \widehat{\boldsymbol{u}}_{j,s}^{k} \\ \widehat{\boldsymbol{u}}_{j,2}^{k} \end{bmatrix} + \begin{bmatrix} \widehat{\boldsymbol{v}}_{j,1}^{k} \\ \widehat{D}_1 \widehat{\boldsymbol{v}}_{j,s}^{k} + \widehat{D}_2 \widehat{\boldsymbol{w}}_{j,s}^{k} \\ \widehat{\boldsymbol{w}}_{j,2}^{k} \end{bmatrix} \text{ for } j = 1, \ldots, N. \tag{2.19}$$

Equations (2.12), (2.17) and (2.19) represent the BJM for each discrete Fourier component $\widehat{\boldsymbol{u}}_j^k$. Clearly the iterative process for each component does not depend on the others, and it suffices to study the convergence of each component separately.

A closer inspection of the matrices in (2.12) and (2.17) reveals that the BJM for one component $\widehat{\boldsymbol{u}}_j^k$ is exactly the BJM for the solution of a discretized one-dimensional $\eta - \Delta$ problem of the form

$$\begin{aligned} \eta_j \widehat{u}_j - \partial_{xx}\widehat{u}_j &= \widehat{f}_j \text{ in } (0,1), \\ \widehat{u}_j(0) = \widehat{u}_j(1) &= 0, \end{aligned} \tag{2.20}$$

where $\widehat{u}_j$ is the jth coefficient of the Fourier sine expansion of u, $\widehat{f}_j$ is the jth Fourier coefficient of f, and $\eta_j = (\pi j)^2$. Hence, if we would know a continuous representation of the BJM for the solution to (2.20), then we could perform a Fourier convergence analysis similarly as it is often done at the continuous level for other one-level domain decomposition methods; see, e.g., [4, 5, 11]. This is exactly the focus of Section 3, where we will show that the BJM for the one-dimensional $\eta - \Delta$ boundary value problem is an OSM. This equivalence will allow us to perform a detailed Fourier convergence analysis of the BJM.

3. Convergence Analysis of the BJM. Motivated by the results in Section 2.3, we study now the BJM for the solution of a one-dimensional discrete $\eta - \Delta$ problem and prove that this is equivalent to a discrete OSM, see for example [23]. Our analysis will reveal that the BJM produces implicitly some particular Robin parameters, dependent on η, in the equivalent OSM. Since the chosen discretization for the OSM is consistent and convergent, one can pass to the limit from the discrete to the continuous level. Therefore, we will obtain that the continuous limit of the BJM is an OSM, where the Robin parameters are the continuous limits of the discrete Robin parameters of the BJM. Once this equivalence interpretation is established, we will study the dependence of the continuous convergence factor of the BJM with respect to η (hence the Fourier frequency), to the size of the overlap, to the number of coarse points and their location.

The main steps of the described analysis are organized in four subsections. In Section 3.1 we recall the OSM, derive its convergence factor at the continuous level and then obtain a discretization based on the finite-difference method for non-uniform grids; see, e.g., [24]. In Section 3.2, we show the equivalence between the BJM and the discrete OSM and discuss the BJM convergence factor in the continuous limit. Sections 3.3 and 3.4 focus on the analysis of the BJM convergence factor for uniform and non-uniform coarse grids.

3.1. The OSM for the one-dimensional $\eta - \Delta$ equation. To recall the OSM for

$$\begin{aligned} &\eta u - u_{xx} = f \text{ in } (0,1),\\ &u(0) = u(1) = 0, \end{aligned} \tag{3.1}$$

we consider an overlapping domain decomposition $(0,1) = (0, \beta := x_\ell) \cup (\alpha := x_m, 1)$; see Figure 2.1 (b), top row. Given an appropriate initialization pair (u_1^0, u_2^0), the OSM for (3.1) is

$$\begin{array}{llll} \eta u_1^k - \partial_{xx} u_1^k = f & \text{in } (0,\beta), & \eta u_2^k - \partial_{xx} u_2^k = f & \text{in } (\alpha,1),\\ u_1^k = 0 & \text{at } x = 0, & u_2^k = 0 & \text{at } x = 1,\\ \partial_x u_1^k + p_{12} u_1^k = \partial_x u_2^{k-1} + p_{12} u_2^{k-1} & \text{at } x = \beta, & \partial_x u_2^k - p_{21} u_2^k = \partial_x u_1^{k-1} - p_{21} u_2^{k-1} & \text{at } x = \alpha, \end{array} \tag{3.2}$$

for $k = 1, 2, \ldots$, where p_{12} and p_{21} are two positive parameters that can be optimized to improve the convergence of the iteration; see, e.g., [11]. This optimization process gives the name *Optimized Schwarz Method* to the scheme (3.2). In fact, the convergence factor of the method depends heavily on p_{12} and p_{21}. To compute this convergence factor, we can assume that $f = 0$ (working by linearity on the error equations). The general solution of the first subproblem in (3.2) with $f = 0$ is of the form $u_1(x) = A_1 e^{\sqrt{\eta}x} + B_1 e^{-\sqrt{\eta}x}$. Using the boundary condition $u_1(0) = 0$, we find that $A_1 = -B_1$ and we thus have $u_1(x) = 2A_1 \sinh(\sqrt{\eta}x)$. Similarly, $u_2(x) = A_2 e^{\sqrt{\eta}x} + B_2 e^{-\sqrt{\eta}x}$, and since $u_2(1) = 0$, we find that $B_2 = -A_2 e^{2\sqrt{\eta}}$ and we thus have $u_2(x) = 2A_2 e^{\sqrt{\eta}} \sinh(\sqrt{\eta}(x-1))$. Using the Robin transmission condition at $x = \alpha$ in the second subproblem of (3.2), we find

$$A_2^k \Big(e^{\sqrt{\eta}} \sqrt{\eta} \cosh(\sqrt{\eta}(\alpha - 1)) - p_{21} e^{\sqrt{\eta}} \sinh(\sqrt{\eta}(\alpha - 1)) \Big) = A_1^{k-1} \Big(\sqrt{\eta} \cosh(\sqrt{\eta}\alpha) - p_{21} \sinh(\sqrt{\eta}\alpha) \Big),$$

which leads to

$$A_2^k = \frac{1}{e^{\sqrt{\eta}}} \frac{\sqrt{\eta}\cosh(\sqrt{\eta}\alpha) - p_{21}\sinh(\sqrt{\eta}\alpha)}{\sqrt{\eta}\cosh(\sqrt{\eta}(\alpha-1)) - p_{21}\sinh(\sqrt{\eta}(\alpha-1))} A_1^{k-1}. \tag{3.3}$$

Similarly, using the Robin condition at the point $x = \beta$ in the first subproblem of (3.2) we find

$$A_1^k = \frac{\sqrt{\eta}\cosh(\sqrt{\eta}(\beta-1)) + p_{12}\sinh(\sqrt{\eta}(\beta-1))}{\sqrt{\eta}\cosh(\sqrt{\eta}\beta) + p_{12}\sinh(\sqrt{\eta}\beta)} e^{\sqrt{\eta}} A_2^{k-1}. \tag{3.4}$$

Replacing A_1^k from (3.4) at iteration $k-1$ into (3.3) shows that the convergence factor over a double iteration of the OSM is

$$\begin{aligned} \rho(\eta, p_{12}, p_{21}, \alpha, \beta) = &\frac{\sqrt{\eta}\cosh(\sqrt{\eta}(1-\beta)) - p_{12}\sinh(\sqrt{\eta}(1-\beta))}{\sqrt{\eta}\cosh(\sqrt{\eta}\beta) + p_{12}\sinh(\sqrt{\eta}\beta)}\\ &\frac{\sqrt{\eta}\cosh(\sqrt{\eta}\alpha) - p_{21}\sinh(\sqrt{\eta}\alpha)}{\sqrt{\eta}\cosh(\sqrt{\eta}(1-\alpha)) + p_{21}\sinh(\sqrt{\eta}(1-\alpha))}. \end{aligned} \tag{3.5}$$

Notice that the convergence factor ρ depends on η, the two Robin parameters p_{12} and p_{21}, and on the positions of the interfaces α and β (hence the length of the overlap $L := \beta - \alpha$).

To obtain a discrete formulation of the OSM, we consider two uniform grids of size h in the subdomains $(0, \beta)$ and $(\alpha, 1)$ as the ones shown in Figure 2.1 (b), top row. Using the finite-difference method applied to these grids, we discretize the two subproblems in (3.2) and obtain the linear systems

$$A_{\mathrm{OSM},1} \boldsymbol{u}_1^k = \boldsymbol{f}_1 + F_1 \boldsymbol{u}_2^{k-1} \quad \text{and} \quad A_{\mathrm{OSM},2} \boldsymbol{u}_2^k = \boldsymbol{f}_2 + F_2 \boldsymbol{u}_1^{k-1}, \tag{3.6}$$

where $A_{\mathrm{OSM},j} \in \mathbb{R}^{(n_j+n_s)\times(n_j+n_s)}$ and $\boldsymbol{f}_j \in \mathbb{R}^{n_j+n_s}$, $j=1,2$, are

$$A_{\mathrm{OSM},1} = \frac{1}{h^2}\begin{bmatrix} 2+\eta h^2 & -1 & & & \\ -1 & 2+\eta h^2 & -1 & & \\ & \ddots & \ddots & \ddots & \\ & & -1 & 2+\eta h^2 & -1 \\ & & & -1 & \frac{2+\eta h^2}{2}+p_{12}h \end{bmatrix},\quad \boldsymbol{f}_1 = \begin{bmatrix} f(x_1) \\ \vdots \\ f(x_\ell) \end{bmatrix}, \tag{3.7}$$

$$A_{\mathrm{OSM},2} = \frac{1}{h^2}\begin{bmatrix} \frac{2+\eta h^2}{2}+p_{21}h & -1 & & & \\ -1 & 2+\eta h^2 & -1 & & \\ & \ddots & \ddots & \ddots & \\ & & -1 & 2+\eta h^2 & -1 \\ & & & -1 & 2+\eta h^2 \end{bmatrix},\quad \boldsymbol{f}_2 = \begin{bmatrix} f(x_m) \\ \vdots \\ f(x_N) \end{bmatrix}, \tag{3.8}$$

and the matrices $F_1 \in \mathbb{R}^{n_1+n_s\times n_2+n_s}$ and $F_2 \in \mathbb{R}^{n_2+n_s\times n_1+n_s}$ are such that

$$F_1\boldsymbol{g} = \begin{bmatrix} 0 \\ \vdots \\ 0 \\ (\frac{p_{12}}{h} - \frac{2+\eta h^2}{2h^2})(\boldsymbol{g})_{n_s} + \frac{1}{h^2}(\boldsymbol{g})_{n_s+1} \end{bmatrix}, \quad F_2\boldsymbol{h} = \begin{bmatrix} (\frac{p_{21}}{h} - \frac{2+\eta h^2}{2h^2})(\boldsymbol{h})_m + \frac{1}{h^2}(\boldsymbol{h})_{m-1} \\ 0 \\ \vdots \\ 0 \end{bmatrix}$$

for any $\boldsymbol{g} \in \mathbb{R}^{n_2+n_s}$ and $\boldsymbol{h} \in \mathbb{R}^{n_1+n_s}$. Notice that, since $\eta, p_{12}, p_{21} > 0$ for any $h > 0$ the matrices $A_{\mathrm{OSM},1}$ and $A_{\mathrm{OSM},2}$ are strictly diagonally dominant, hence invertible. Therefore, the OSM (3.6) is a stationary method whose standard form (see, e.g., [6]) is

$$\begin{bmatrix} \boldsymbol{u}_1^k \\ \boldsymbol{u}_2^k \end{bmatrix} = M_{\mathrm{OSM}}^{-1}N_{\mathrm{OSM}}\begin{bmatrix} \boldsymbol{u}_1^{k-1} \\ \boldsymbol{u}_2^{k-1} \end{bmatrix} + M_{\mathrm{OSM}}^{-1}\begin{bmatrix} \boldsymbol{f}_1 \\ \boldsymbol{f}_2 \end{bmatrix}, \tag{3.9}$$

where $M_{\mathrm{OSM}} = \begin{bmatrix} A_{\mathrm{OSM},1} & 0 \\ 0 & A_{\mathrm{OSM},2} \end{bmatrix}$ and $N_{\mathrm{OSM}} = \begin{bmatrix} 0 & F_1 \\ F_2 & 0 \end{bmatrix}$. This is sometimes also called an optimized block Jacobi algorithm; see, e.g., [23]. If convergent, this iterative procedure generates a sequence that converges to the solution of the augmented problem

$$\begin{bmatrix} A_{\mathrm{OSM},1} & -F_1 \\ -F_2 & A_{\mathrm{OSM},2} \end{bmatrix}\begin{bmatrix} \boldsymbol{u}_1 \\ \boldsymbol{u}_2 \end{bmatrix} = \begin{bmatrix} \boldsymbol{f}_1 \\ \boldsymbol{f}_2 \end{bmatrix}.$$

In our analysis, another equivalent form of the the discrete OSM (3.9) will play a crucial role. This is the so-called optimized restricted additive Schwarz (ORAS) method, which is defined as

$$\widehat{\boldsymbol{u}}^{k+1} = \widehat{\boldsymbol{u}}^k + \widetilde{R}_1^\top A_{\mathrm{OSM},1}^{-1}R_1\widehat{\boldsymbol{r}}^k + \widetilde{R}_2^\top A_{\mathrm{OSM},2}^{-1}R_2\widehat{\boldsymbol{r}}^k, \tag{3.10}$$

where $\widehat{\boldsymbol{r}}^k = \boldsymbol{f} - A\widehat{\boldsymbol{u}}^k$, $R_1 \in \mathbb{R}^{(n_1+n_s)\times N}$, and $R_2 \in \mathbb{R}^{(n_2+n_s)\times N}$ are restriction matrices of the form

$$R_1 = \begin{bmatrix} I_{n_1} & 0 & 0 \\ 0 & I_{n_s} & 0 \end{bmatrix} \text{ and } R_2 = \begin{bmatrix} 0 & I_{n_s} & 0 \\ 0 & 0 & I_{n_2} \end{bmatrix}, \tag{3.11}$$

while $\widetilde{R}_1 \in \mathbb{R}^{(n_1+n_s)\times N}$ and $\widetilde{R}_2 \in \mathbb{R}^{(n_2+n_s)\times N}$ are similar restriction matrices, but corresponding to a non-overlapping decomposition satisfying $\widetilde{R}_1^\top\widetilde{R}_1 + \widetilde{R}_2^\top\widetilde{R}_2 = I_N$; see [23] for more details. It is proved in [23] that (3.10) and (3.9) are equivalent for any R_1 and R_2, as the ones considered in this section, that induce a consistent matrix splitting.

3.2. The BJM as an OSM for the one-dimensional $\eta - \Delta$ equation. Let us first recall the BJM for the one-dimensional problem (3.1) and state explicitly all the matrices that we need for our analysis. We consider the grids shown in Figure 2.1 (b) and the finite-difference method for non-uniform grids; see, e.g., [24]. The full problem on the global fine mesh (Figure 2.1 (b), top row) is

$$A\boldsymbol{u} = \boldsymbol{f}, \tag{3.12}$$

where $A \in \mathbb{R}^{N\times N}$ is a tridiagonal symmetric matrix that we decompose as

$$A = \begin{bmatrix} A_1 & B_1 & 0 \\ B_1^\top & A_s & B_2^\top \\ 0 & B_2 & A_2 \end{bmatrix}. \tag{3.13}$$

The matrices $A_1 \in \mathbb{R}^{n_1\times n_1}$, $A_s \in \mathbb{R}^{n_s\times n_s}$, and $A_2 \in \mathbb{R}^{n_2\times n_2}$, are tridiagonal and have the form

$$\frac{1}{h^2}\begin{bmatrix} 2+\eta h^2 & -1 & & \\ -1 & 2+\eta h^2 & -1 & \\ & \ddots & \ddots & \ddots \end{bmatrix},$$

while $B_1 \in \mathbb{R}^{n_1\times n_s}$ and $B_2 \in \mathbb{R}^{n_2\times n_s}$ are zero except for one corner entry:

$$B_1 = \frac{1}{h^2}\begin{bmatrix} \vdots & \vdots & \vdots & \vdots \\ 0 & 0 & \cdots & 0 \\ -1 & 0 & \cdots & 0 \end{bmatrix} \text{ and } B_2 = \frac{1}{h^2}\begin{bmatrix} 0 & \cdots & 0 & -1 \\ 0 & \cdots & 0 & 0 \\ \vdots & \vdots & \vdots & \vdots \end{bmatrix}.$$

Hence for a given approximation $\boldsymbol{u}^k = [(\boldsymbol{u}_1^k)^\top, (\boldsymbol{u}_s^k)^\top, (\boldsymbol{u}_s^k)^\top]^\top$, the residual $\boldsymbol{r}^k$ is

$$\boldsymbol{r}^k = \begin{bmatrix} \boldsymbol{r}_1^k \\ \boldsymbol{r}_s^k \\ \boldsymbol{r}_s^k \end{bmatrix} = \begin{bmatrix} \boldsymbol{f}_1 \\ \boldsymbol{f}_s \\ \boldsymbol{f}_s \end{bmatrix} - \begin{bmatrix} A_1 & B_1 & 0 \\ B_1^\top & A_s & B_2^\top \\ 0 & B_2 & A_2 \end{bmatrix}\begin{bmatrix} \boldsymbol{u}_1^k \\ \boldsymbol{u}_s^k \\ \boldsymbol{u}_s^k \end{bmatrix}. \tag{3.14}$$

The correction problems on the two partially coarse grids (Figure 2.1 (b), middle and bottom rows), are

$$A_{\Omega_1}\boldsymbol{v}^k = T_2\boldsymbol{r}^k \quad \text{and} \quad A_{\Omega_2}\boldsymbol{w}^k = T_1\boldsymbol{r}^k, \tag{3.15}$$

where $A_{\Omega_1} \in \mathbb{R}^{(n_1+n_s+m_2)\times(n_1+n_s+m_2)}$, $A_{\Omega_2} \in \mathbb{R}^{(n_2+n_s+m_1)\times(n_2+n_s+m_1)}$, $T_1 \in \mathbb{R}^{(n_2+n_s+m_1)\times N}$, and $T_2 \in \mathbb{R}^{(n_1+n_s+m_2)\times N}$ have the forms given in (2.3), with A_1, A_s, A_2, B_1, and B_2 as above. The matrices $C_1 \in \mathbb{R}^{n_s\times m_1}$ and $C_2 \in \mathbb{R}^{n_s\times m_2}$ are

$$C_1 = \frac{1}{h^2}\begin{bmatrix} 0 & \cdots & 0 & -1 \\ 0 & \cdots & 0 & 0 \\ \vdots & \vdots & \vdots & \vdots \end{bmatrix} \text{ and } C_2 = \frac{1}{h^2}\begin{bmatrix} \vdots & \vdots & \vdots & \vdots \\ 0 & 0 & \cdots & 0 \\ -1 & 0 & \cdots & 0 \end{bmatrix}.$$

The matrices $\widetilde{A}_1 \in \mathbb{R}^{m_1 \times m_1}$ and $\widetilde{B}_1 \in \mathbb{R}^{m_1 \times n_s}$ in the BJM method in Algorithm 2.1 are

$$\widetilde{A}_1 = \frac{1}{h_2^2}\begin{bmatrix} 2+\eta h_2^2 & -1 & & & \\ -1 & 2+\eta h_2^2 & -1 & & \\ & \ddots & \ddots & \ddots & \\ & & -1 & 2+\eta h_2^2 & -1 \\ & & & \frac{-2h_2}{h+h_2} & \frac{2h_2}{h}+\eta h_2^2 \end{bmatrix} \text{ and } \widetilde{B}_1 = \begin{bmatrix} \vdots & \vdots & \vdots & \vdots \\ 0 & 0 & \cdots & 0 \\ \frac{-2}{h(h+h_2)} & 0 & \cdots & 0 \end{bmatrix},$$

while $\widetilde{A}_2 \in \mathbb{R}^{m_2 \times m_2}$ and $\widetilde{B}_2 \in \mathbb{R}^{m_2 \times n_s}$ are

$$\widetilde{A}_2 = \frac{1}{h_1^2}\begin{bmatrix} \frac{2h_1}{h}+\eta h_1^2 & \frac{-2h_1}{h+h_1} & & & \\ -1 & 2+\eta h_1^2 & -1 & & \\ & \ddots & \ddots & \ddots & \\ & & -1 & 2+\eta h_1^2 & -1 \\ & & & -1 & 2+\eta h_1^2 \end{bmatrix} \text{ and } \widetilde{B}_2 = \begin{bmatrix} 0 & \cdots & 0 & \frac{-2}{h(h+h_1)} \\ 0 & \cdots & 0 & 0 \\ \vdots & \vdots & \vdots & \vdots \end{bmatrix}.$$

We do not need to specify the restriction matrices M_1 and M_2, because they multiply the residual components $\boldsymbol{r}_1$ and $\boldsymbol{r}_2$, which are zero as shown in the upcoming Lemma 3.1. The matrices M_j do not play any role in the convergence of the method if our new partition of unity is used. However, if the original partition of unity proposed in [1] is considered, then they contributes to the convergence behavior. Finally, the partition of unity diagonal matrices $D_1 \in \mathbb{R}^{n_s \times n_s}$ and $D_2 \in \mathbb{R}^{n_s \times n_s}$ have the structures given in (2.4). Notice that, since $\eta > 0$, the tridiagonal matrices $\widetilde{A}_{\Omega_1}$ and $\widetilde{A}_{\Omega_1}$ are strictly diagonally dominant for any $h, h_1, h_2 > 0$, hence invertible.

The BJM in Algorithm 2.1 consists of iteratively computing the residual (3.14), solving the two correction problems (3.15) and then computing the new approximation using (2.5). We are now ready to prove the equivalence between the BJM and the discrete OSM. To do so, we need an important property of the BJM proved in the next lemma.

LEMMA 3.1. *The BJM for the solution of* (3.12) *(and based on* (3.14)*,* (3.15)*, and* (2.5) *with all the matrices described above) produces for any initial guess* $\boldsymbol{u}^0$ *and arbitrary partitions of unity satisfying* (2.4) *zero residual components outside the overlap,* $\boldsymbol{r}_1^k = \boldsymbol{r}_2^k = 0$*, for* $k = 1, 2, \dots$

Proof. We only sketch the proof here, since the result is proved in detail in [7]. Moreover, we consider only $\boldsymbol{r}_1^k$, because the proof for $\boldsymbol{r}_2^k$ is similar. Using equations (3.14) and (2.5), we compute

$$\begin{aligned} \boldsymbol{r}_1^k &= \boldsymbol{f}_1 - (A_1\boldsymbol{u}_1^k + B_1\boldsymbol{u}_s^k) \\ &= \boldsymbol{f}_1 - A_1(\boldsymbol{u}_1^{k-1} + \boldsymbol{v}_1^{k-1}) - B_1(\boldsymbol{u}_s^{k-1} + D_1\boldsymbol{v}_s^{k-1} + D_2\boldsymbol{w}_s^{k-1}) \\ &= \boldsymbol{r}_1^{k-1} - A_1\boldsymbol{v}_1^{k-1} - B_1(D_1\boldsymbol{v}_s^{k-1} + D_2\boldsymbol{w}_s^{k-1}) \\ &= B_1\boldsymbol{v}_s^k - B_1(D_1\boldsymbol{v}_s^{k-1} + D_2\boldsymbol{w}_s^{k-1}), \end{aligned}$$

since $\boldsymbol{r}_1^{k-1} - A_1\boldsymbol{v}_1^{k-1} = B_1\boldsymbol{v}_s^{k-1}$ because of equation (3.15) at $k-1$. Now using the structures of B_1, D_1 and D_2 we get

$$B_1 D_1 \boldsymbol{v}_s^{k-1} = \frac{1}{h^2}\begin{bmatrix} \vdots & \vdots & \vdots & \vdots \\ 0 & 0 & \cdots & 0 \\ -1 & 0 & \cdots & 0 \end{bmatrix}\begin{bmatrix} 1 & & & \\ & \times & & \\ & & \ddots & \\ & & & \times \\ & & & & 0 \end{bmatrix}\begin{bmatrix} (\boldsymbol{v}_{s,1})^{k-1} \\ \vdots \\ (\boldsymbol{v}_{s,n_s})^{k-1} \end{bmatrix} = \frac{1}{h^2}\begin{bmatrix} 0 \\ \vdots \\ 0 \\ (\boldsymbol{v}_{s,1})^{k-1} \end{bmatrix},$$

independently of the middle elements of D_1[4], and thus $B_1\boldsymbol{v}_s^{k-1} - B_1 D_1 \boldsymbol{v}_s^{k-1} = 0$. By a similarly calculation, one can show that $B_1 D_2 \boldsymbol{w}_s^{k-1} = 0$, also independently of the middle elements of D_2, which proves that $\boldsymbol{r}_1^k = 0$ for $k = 1, 2, \ldots$ ∎

Since $\widetilde{A}_1$ and $\widetilde{A}_2$ are invertible, the Schur-complement matrices $A_s - C_2\widetilde{A}_2^{-1}\widetilde{B}_2$ (of A_{Ω_1}) and $A_s - C_1\widetilde{A}_1^{-1}\widetilde{B}_1$ (of A_{Ω_2}) are well-defined and we can compute the entries we need for our analysis using the following lemma.

LEMMA 3.2. *The first element of the inverse of the $n \times n$ tridiagonal matrix*

$$T = \begin{bmatrix} a_1 & b_1 & & \\ -1 & a & -1 & \\ & \ddots & \ddots & \ddots \\ & & -1 & a \end{bmatrix} \tag{3.16}$$

is given by $\mu(n) := (T^{-1})_{1,1} = \frac{\lambda_2^n - \lambda_1^n}{\lambda_2^n(a_1+b_1\lambda_1) - \lambda_1^n(a_1+b_1\lambda_2)}$, $\lambda_{1,2} := \frac{a}{2} \pm \sqrt{\frac{a^2}{4} - 1}$.

Proof. The first element of the inverse of T is the first component u_1 of the solution of the linear system

$$T\boldsymbol{u} = \begin{bmatrix} a_1 & b_1 & & \\ -1 & a & -1 & \\ & \ddots & \ddots & \ddots \\ & & -1 & a \end{bmatrix} \begin{bmatrix} u_1 \\ u_2 \\ \vdots \\ u_n \end{bmatrix} = \begin{bmatrix} 1 \\ 0 \\ \vdots \\ 0 \end{bmatrix}.$$

The solution satisfies the recurrence relation $-u_{j+1} + a u_j - u_{j-1} = 0$, $j = 2, 3, \ldots, n-1$, whose general solution is $u_j = C_1\lambda_1^j + C_2\lambda_2^j$ with $\lambda_{1,2}$ the characteristic roots of $\lambda^2 - a\lambda + 1 = 0$ given in the statement of the lemma. The two boundary conditions to determine the constants $C_{1,2}$ are

$$\begin{aligned} a_1u_1 + b_1u_2 &= a_1(C_1\lambda_1 + C_2\lambda_2) + b_1(C_1\lambda_1^2 + C_2\lambda_2^2) = 1, \\ -u_{n-1} + au_n &= -(C_1\lambda_1^{n-1} + C_2\lambda_2^{n-1}) + a(C_1\lambda_1^n + C_2\lambda_2^n) = 0. \end{aligned}$$

Solving this linear system for $C_{1,2}$ gives (using that $3 - i = 2$ if $i = 1$ and $3 - i = 1$ if $i = 2$)

$$C_i = \frac{a\lambda_{3-i}^n - \lambda_{3-i}^{n-1}}{(a_1\lambda_1 + b_1\lambda_1^2)(a\lambda_2^n - \lambda_2^{n-1}) + (a_1\lambda_2 + b_1\lambda_2^2)(\lambda_1^{n-1} - a\lambda_1^n)}, \quad i = 1, 2. \tag{3.17}$$

Inserting these constants into u_j and evaluating at $j = 1$ gives

$$u_1 = \frac{\lambda_2^{n-2}(a\lambda_2 - 1) - \lambda_1^{n-2}(a\lambda_1 - 1)}{\lambda_2^{n-2}(a_1 + b_1\lambda_1)(a\lambda_2 - 1) - \lambda_1^{n-2}(a_1 + b_1\lambda_2)(a\lambda_1 - 1)},$$

which upon simplification, using the Vieta relations satisfied by the roots, i.e. $\lambda_1\lambda_2 = 1$ and $\lambda_1 + \lambda_2 = a$, leads to the result. ∎

[4]The 1 in the partitions of unity D_1 and D_2 is however very important, see [7], and for more details on whether partition of unity functions influence the convergence of Schwarz methods, see [13].

Lemma 3.3. *The matrices* $C_2\widetilde{A}_2^{-1}\widetilde{B}_2$ *and* $C_1\widetilde{A}_1^{-1}\widetilde{B}_1$ *are given by*

$$C_2\widetilde{A}_2^{-1}\widetilde{B}_2 = \begin{bmatrix} 0 & & & \\ & \ddots & & \\ & & 0 & \\ & & & \frac{h_1^2}{h^2}\frac{2\mu(m_2)}{h(h+h_1)} \end{bmatrix}, \quad C_1\widetilde{A}_1^{-1}\widetilde{B}_1 = \begin{bmatrix} \frac{h_2^2}{h^2}\frac{2\mu(m_1)}{h(h+h_2)} & & & \\ & 0 & & \\ & & \ddots & \\ & & & 0 \end{bmatrix},$$

with the function $\mu(n)$ *from Lemma 3.2.*

Proof. For the first result, using the sparsity patterns of C_2 and $\widetilde{B}_2$, we obtain

$$C_2\widetilde{A}_2^{-1}\widetilde{B}_2 = \begin{bmatrix} & \\ & \\ \frac{-1}{h^2} & \end{bmatrix} \widetilde{A}_2^{-1} \begin{bmatrix} & \frac{-2}{h(h+h_1)} \\ & \\ & \end{bmatrix} = \frac{1}{h^2}\begin{bmatrix} 0 & & \\ & \ddots & \\ & & \frac{2(\widetilde{A}_2^{-1})_{11}}{h(h+h_1)} \end{bmatrix},$$

and we thus need to find the first entry of $\widetilde{A}_2^{-1}$. Defining $a_1 := \frac{2h_1}{h} + \eta h_1^2$, $b_1 := \frac{-2h_1}{h+h_1}$, and $a := 2 + \eta h_1^2$, and multiplying by h_1^2, we obtain precisely a matrix like in Lemma 3.2,

$$h_1^2\widetilde{A}_2 = \begin{bmatrix} a_1 & b_1 & & & \\ -1 & a & -1 & & \\ & \ddots & \ddots & \ddots & \\ & & -1 & a & -1 \\ & & & -1 & a \end{bmatrix},$$

and therefore $((h_1^2\widetilde{A}_2)^{-1})_{11} = \mu(m_2)$, which shows the first claim. For the second one, it suffices to notice that Lemma 3.2 also holds if the matrix is reordered from top left to bottom right, and can thus be used again. ∎

Now, using the Schur-complements $A_s - C_2\widetilde{A}_2^{-1}\widetilde{B}_2$ (of A_{Ω_1}) and $A_s - C_1\widetilde{A}_1^{-1}\widetilde{B}_1$ (of A_{Ω_2}), we can introduce the matrices $\widehat{A}_1$ and $\widehat{A}_2$:

$$\widehat{A}_1 := \begin{bmatrix} A_1 & B_1 \\ B_1^\top & A_s - C_2\widetilde{A}_2^{-1}\widetilde{B}_2 \end{bmatrix} \text{ and } \widehat{A}_2 := \begin{bmatrix} A_s - C_1\widetilde{A}_1^{-1}\widetilde{B}_1 & B_2^\top \\ B_2 & A_2 \end{bmatrix}, \tag{3.18}$$

which allow us to prove the following result.

Lemma 3.4. *The matrices* $\widehat{A}_1$ *and* $\widehat{A}_2$ *are invertible and the inverses of* A_{Ω_1} *and* A_{Ω_2} *have the forms*

$$A_{\Omega_1}^{-1} = \begin{bmatrix} \widehat{A}_1^{-1} & 0 \\ -\overline{B}_1\widehat{A}_1^{-1} & I_{m_2} \end{bmatrix} \begin{bmatrix} I_{n_1} & 0 & 0 \\ 0 & I_{n_s} & -C_2\widetilde{A}_2^{-1} \\ 0 & 0 & \widetilde{A}_2^{-1} \end{bmatrix} \tag{3.19}$$

and

$$A_{\Omega_2}^{-1} = \begin{bmatrix} I_{m_2} & -\overline{B}_2\widehat{A}_2^{-1} \\ 0 & \widehat{A}_2^{-1} \end{bmatrix} \begin{bmatrix} \widetilde{A}_1^{-1} & 0 & 0 \\ -C_2\widetilde{A}_2^{-1} & I_{n_s} & 0 \\ 0 & 0 & I_{n_2} \end{bmatrix}, \tag{3.20}$$

where $\overline{B}_1 = [0\ ,\ \widetilde{A}_2^{-1}\widetilde{B}_2]$ *and* $\overline{B}_2 = [\widetilde{A}_1^{-1}\widetilde{B}_1\ ,\ 0]$.

Proof. We prove the result for $\widehat{A}_1$. The proof for $\widehat{A}_2$ can be obtained exactly by the same arguments. Recalling that $\eta > 0$, a direct inspection of the matrix A_{Ω_1} reveals that it is strictly diagonally dominant. Hence, $\det(A_{\Omega_1}) \neq 0$. Now, consider the block structure of A_{Ω_1} given in (2.3). Since $\widetilde{A}_2$ is invertible, we factorize A_{Ω_1} as

$$\begin{bmatrix} A_1 & B_1 & 0 \\ B_1^\top & A_s & C_2 \\ 0 & \widetilde{B}_2 & \widetilde{A}_2 \end{bmatrix} = \begin{bmatrix} I_{n_1} & 0 & 0 \\ 0 & I_{n_s} & C_2 \\ 0 & 0 & \widetilde{A}_2 \end{bmatrix} \begin{bmatrix} A_1 & B_1 & 0 \\ B_1^\top & A_s - C_2\widetilde{A}_2^{-1}\widetilde{B}_2 & 0 \\ 0 & \widetilde{A}_2^{-1}\widetilde{B}_2 & I_{m_2} \end{bmatrix},$$

where I_{n_1}, I_{n_s}, and I_{m_2} are identity matrices of sizes n_1, n_s, and m_2. This factorization allows us to write $0 \neq \det(A_{\Omega_1}) = \det(\widetilde{A}_2)\det(\widehat{A}_1)$, which implies that $\det(\widehat{A}_1) \neq 0$. Now, a straightforward calculation using the previous factorization allows us to get (3.19). ∎

Now, we notice that the BJM can be written (using (3.15) and (2.5)) in the compact form

$$\boldsymbol{u}^{k+1} = \boldsymbol{u}^k + \widetilde{T}_1 A_{\Omega_1}^{-1} T_1 \boldsymbol{r}^k + \widetilde{T}_2 A_{\Omega_2}^{-1} T_2 \boldsymbol{r}^k, \tag{3.21}$$

where the block-diagonal matrices $\widetilde{T}_1 \in \mathbb{R}^{(n_1+n_s+m_2)\times N}$ and $\widetilde{T}_2 \in \mathbb{R}^{(m_1+n_s+n_2)\times N}$ are

$$\widetilde{T}_1 = \begin{bmatrix} I_{n_1} & 0 & 0 \\ 0 & D_1 & 0 \\ 0 & 0 & 0 \end{bmatrix} \text{ and } \widetilde{T}_2 = \begin{bmatrix} 0 & 0 & 0 \\ 0 & D_2 & 0 \\ 0 & 0 & I_{n_2} \end{bmatrix}.$$

A direct calculation using Lemma 3.1 (hence that $\boldsymbol{r}_1^k = 0$ and $\boldsymbol{r}_2^k = 0$) and Lemma 3.4 (hence the formulas (3.19) and (3.20)) allows us to obtain

$$\widetilde{T}_1 A_{\Omega_1}^{-1} T_1 \boldsymbol{r}^k = \begin{bmatrix} I_{n_1} & 0 \\ 0 & D_1 \\ 0 & 0 \end{bmatrix} \widehat{A}_1^{-1} R_1 \boldsymbol{r}^k \text{ and } \widetilde{T}_2 A_{\Omega_2}^{-1} T_2 \boldsymbol{r}^k = \begin{bmatrix} 0 & 0 \\ D_2 & 0 \\ 0 & I_{n_2} \end{bmatrix} \widehat{A}_2^{-1} R_2 \boldsymbol{r}^k,$$

where the matrices R_1 and R_2 are the ones given in (3.11). Since the results proved in Lemma 3.1 are independent of the middle diagonal entries of D_1 and D_2, we can choose them such that the equalities

$$\widetilde{R}_1^\top = \begin{bmatrix} I_{n_1} & 0 \\ 0 & D_1 \\ 0 & 0 \end{bmatrix} \text{ and } \widetilde{R}_2^\top = \begin{bmatrix} 0 & 0 \\ D_2 & 0 \\ 0 & I_{n_2} \end{bmatrix} \tag{3.22}$$

are fulfilled. Therefore, the BJM (3.21) becomes

$$\boldsymbol{u}^{k+1} = \boldsymbol{u}^k + \widetilde{R}_1^\top \widehat{A}_1^{-1} R_1 \boldsymbol{r}^k + \widetilde{R}_2^\top \widehat{A}_2^{-1} R_2 \boldsymbol{r}^k, \tag{3.23}$$

which is already very similar to the ORAS method (3.10). Now, a direct comparison of $\widehat{A}_1$ and $A_{\text{OSM},1}$, which uses the results of Lemma 3.3, reveals that they are equal except for the bottom-right corner elements, which are

$$\begin{aligned} (A_{\text{OSM},1})_{n_1+n_s,n_1+n_s} &= \frac{2+\eta h^2}{2h^2} + \frac{p_{12}}{h}, \\ (\widehat{A}_1)_{n_1+n_s,n_1+n_s} &= \frac{2+\eta h^2}{h^2} - \frac{2h_1^2}{h^3(h+h_1)}\mu(m_2). \end{aligned} \tag{3.24}$$

Similarly, $\widehat{A}_2$ and $A_{\mathrm{OSM},2}$ are equal except for the top-left corner elements, which are

$$(A_{\mathrm{OSM},2})_{1,1} = \frac{2+\eta h^2}{2h^2} + \frac{p_{21}}{h}, \qquad (\widehat{A}_2)_{1,1} = \frac{2+\eta h^2}{h^2} - \frac{2h_2^2}{h^3(h+h_2)}\mu(m_1). \tag{3.25}$$

Therefore, if one chooses

$$p_{12} := \frac{2+\eta h^2}{2h} - \frac{2h_1^2}{h^2(h+h_1)}\mu(m_2) \quad \text{and} \quad p_{21} := \frac{2+\eta h^2}{2h} - \frac{2h_2^2}{h^2(h+h_2)}\mu(m_1), \tag{3.26}$$

then $\widehat{A}_j = A_{\mathrm{OSM},j}$ for $j = 1, 2$. Replacing this equality into (3.23), we obtain that the BJM is equivalent to the ORAS method (3.10), and hence to the discrete OSM (3.6). We summarize our findings in the following theorem.

THEOREM 3.5. *If the partition of unity matrices D_1 and D_2 have the forms* (2.4) *and are chosen such that the equalities* (3.22) *hold, and if the Robin parameters of the discrete OSM* (3.6) *are chosen as in* (3.26)*, then the BJM is equivalent to the ORAS method* (3.10) *and to the discrete OSM* (3.6).

Notice that Theorem 3.5 has the following important consequence. Since the discrete OSM (3.6) is obtained by a consistent and convergent discretization of the continuous OSM (3.2), we find that, in the limit for $h \to 0$, the continuous counterpart of the BJM is the OSM (3.2). This will allow us to study in Section 3.3 and 3.4 the convergence factor of the BJM at the continuous level. For this purpose, from now on, we denote by $p_{12}(h, \eta, h_1)$ and $p_{21}(h, \eta, h_2)$ the two Robin parameters of (3.26) to stress their dependence on the discretization size h, the (Fourier) parameter η and the coarse mesh sizes h_1 and h_2. Notice that $\mu(m_2)$ and $\mu(m_1)$ in (3.26) depend on h, h_1, h_2 and η (see Lemma 3.3). Recalling the results obtained in Section 3.1, the continuous BJM convergence factor is given by (3.5), where p_{12} and p_{21} are the limits for $h \to 0$ (with m_1 and m_2 fixed) of the parameters chosen in Theorem 3.5.

It is important to remark at this point that the first coarse points, namely the point (n_1+n_2+1) for the first mesh and the point m_1 for the second mesh, are located at distance h from the interfaces. With this choice we were able to define discrete finite-difference derivatives across these points and in Sections 3.3 and 3.4 we will take limits for $h \to 0$, while keeping the numbers m_1 and m_2 of the coarse points fixed.

Finally, we wish to remark that all the calculations performed in this section, except for the precise formulas for $\mu(m_2)$ and $\mu(m_1)$ in Lemma 3.3, remain valid if, instead of uniform coarse grids, one considers two coarse grids which are non-uniform, in the sense that the m_1 points in $\Omega_1 \setminus \Omega_2$ and the m_2 points in $\Omega_2 \setminus \Omega_1$ are not uniformly distributed, leading to invertible matrices $\widetilde{A}_1$ and $\widetilde{A}_2$. Therefore, the equivalence between BJM and OSM remains valid also in the case of non-uniform coarse grids.

3.3. Uniform coarse grid. The goal of this section is to study the contribution of uniform coarse grids to the convergence of the BJM for the solution to (2.6). For simplicity, we assume that the two partially coarse grids have the same number of coarse points $m := m_1 = m_2$. To satisfy this condition, we fix the size of the overlap L and choose $\alpha = \frac{1-L}{2}$ and $\beta = \frac{1+L}{2}$. In this case, we also have that $h_1 = h_2 = \frac{1-\beta-h}{m}$. We consider the cases of $m = 2$, $m = 3$, and $m = 4$ coarse points.

For the sake of clarity, we first summarize the structure of our analysis. For each given $m \in \{2, 3, 4\}$, we first consider the corresponding BJM Robin parameters, whose explicit formulas can be obtained as in Lemma 3.3, and then pass to the limit for $h \to 0$ to get their continuous counterparts. These continuous parameters will be replaced into the formula (3.5), which will give us the continuous convergence factor of the BJM corresponding to the given m, to a fixed (Fourier) parameter η, and to the size of the overlap L. For fixed m and given values of L we will numerically compute the maximum of the convergence factor with respect to the (Fourier) parameter η. This will allow us to study the deterioration of the contraction factor for decreasing size L of the overlap. While performing this analysis, we compare the convergence of the BJM to the one of the OSM with optimized parameter.

From the convergence factor ρ of the OSM in (3.5), we see that choosing

$$p_{12}^* = \sqrt{\eta}\coth(\sqrt{\eta}(1-\beta)) \quad \text{and} \quad p_{21}^* = \sqrt{\eta}\coth(\sqrt{\eta}\alpha) \tag{3.27}$$

gives $\rho = 0$ for the frequency η. These are thus the optimal parameters for this frequency, and make the OSM a direct solver for the corresponding error component.

For $m = 2$ coarse points, proceeding as in the proof of Lemma 3.2 to compute the corresponding $\mu(m_2) = \mu(m_1)$ and using (3.26), we get the (discrete) BJM Robin parameters

$$\begin{aligned} &p_{12} = \frac{1}{h} + \frac{\eta h}{2} - hE_2(h_1) \quad \text{and} \quad p_{21} = \frac{1}{h} + \frac{\eta h}{2} - hE_2(h_2), \\ &E_2(\tilde{h}) := \frac{2(\eta\tilde{h}^2 + 2)\tilde{h}}{h^2(\eta^2 h^2 \tilde{h}^3 + \eta^2 h\tilde{h}^4 + 2\eta h^2\tilde{h} + 4\eta h\tilde{h}^2 + 2\eta\tilde{h}^3 + 2h + 4\tilde{h})}. \end{aligned} \tag{3.28}$$

Recalling that $h_1 = h_2 = \frac{1-\beta-h}{2}$ and taking the limit for $h \to 0$, we obtain

$$\hat{p}_{12} := \lim_{h\to 0} p_{12} = R_2(1-\beta), \quad \hat{p}_{21} := \lim_{h\to 0} p_{21} = R_2(\alpha), \quad R_2(\tilde{L}) := \frac{\tilde{L}^4\eta^2 + 16\tilde{L}^2\eta + 32}{4\tilde{L}^3\eta + 32\tilde{L}}. \tag{3.29}$$

We see that the Robin parameters $\hat{p}_{12}$ and $\hat{p}_{21}$ are rational functions of the Fourier parameter η with coefficients depending on the outer subdomain sizes $1 - \beta$ and α. In Figure 3.1, we compare the Robin parameter $\hat{p}_{12}$ of the BJM for $m = 2$ (blue line) with the optimal Robin parameter p_{12}^* of the OSM (black dashed line) for three different values of the overlap L. We observe that for small η the Robin parameters of both methods are quite close, which indicates that the BJM method performs well for low-frequency error components. This is clearly visible in Figure 3.2, where we plot the corresponding convergence factors (as functions of η) inserting $\hat{p}_{12}$ and $\hat{p}_{12}$ into (3.5)[5] for two different overlaps L, using $\alpha = \frac{1-L}{2}$ and $\beta = \frac{1+L}{2}$. We also see that the convergence factor clearly has a maximum at some $\eta_2(L)$, whose corresponding error mode converges most slowly, and convergence deteriorates when L becomes small. In Figure 3.3 (left), we present the value $\eta_2(L)$ as functions of L and observe that it grows like $O(L^{-1})$. The corresponding contraction factor, namely $\bar{\rho}_2(L) := \max_\eta \rho_2(\eta, L) := \max_\eta \rho(\eta, \hat{p}_{12}(\eta, L), \hat{p}_{21}(\eta, L), \alpha = \frac{1-L}{2}, \beta = \frac{1+L}{2})$, is shown as function of L in Figure 3.3 (right-dashed blue line, represented as $1 - \rho_2(L)$). Here, one can observe clearly that as L gets smaller the convergence deteriorates with an order $O(L^{1/2})$.

Let us now discuss the behavior $\bar{\rho}_2(L) = 1 - O(L^{\frac{1}{2}})$ shown in Figure 3.3 (right): it was proved in [11] that the convergence factor of the OSM with overlap L behaves like $\rho_{OSM}^\star = 1 - O(L^{\frac{1}{3}})$ with

[5]To evaluate the convergence factor numerically one needs to factor out an exponential in the hyperbolic trigonometric functions to avoid overflow.

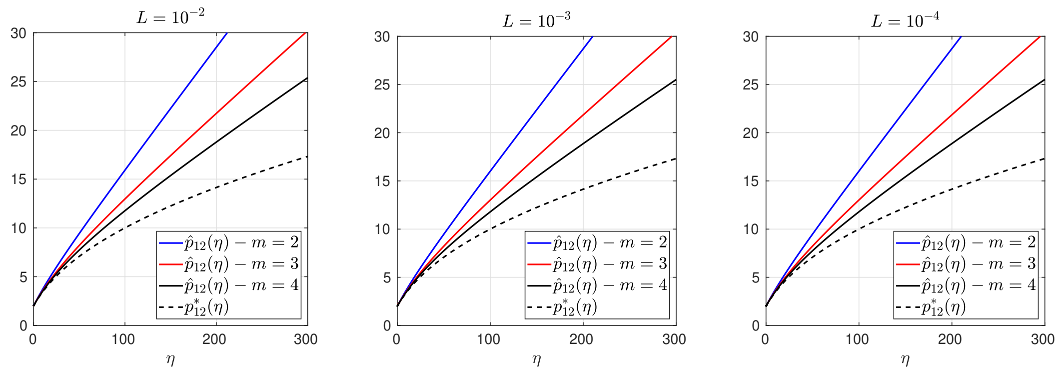

Fig. 3.1: Comparison of the Robin parameters p^*_{12} of the OSM and $\hat{p}_{12}$ of the BJM for $m = 2, 3, 4$ (uniformly distributed) coarse points and overlap $L = 10^{-2}$ (left), $L = 10^{-3}$ (middle), $L = 10^{-4}$ (right).

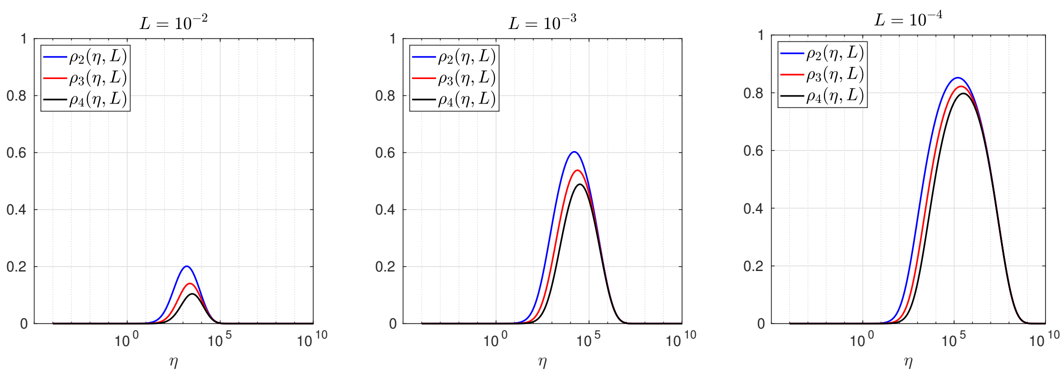

Fig. 3.2: Convergence factors $\rho_m(\eta, L)$ as functions of η and for $m = 2, 3, 4$ (uniformly distributed) coarse points and $L = 10^{-2}$ (left), $L = 10^{-3}$ (middle), $L = 10^{-4}$ (right).

Robin transmission conditions, and $\rho^\star_{OSM} = 1 - O(L^{\frac{1}{5}})$ with second-order (Ventcell) transmission conditions. Hence, the OSM performs better than the BJM with a uniform coarse grid with $m = 2$ uniformly distributed coarse points[6], since convergence deteriorates more slowly when the overlap L goes to zero.

We have seen that, for only two points the BJM is already a good method for low frequencies, since the parameters $\hat{p}_{12}$ and $\hat{p}_{21}$ are very close to the optimal ones p^*_{12} and p^*_{21} for relatively small η. However, the convergence factor deteriorates with L faster than for the OSM. It is natural to ask: does the behavior of the BJM improve if more coarse points are used? The answer is surprisingly negative! In fact, the convergence factor remains of order $1 - O(L^{\frac{1}{2}})$. To see this, we now repeat

[6]Note that one of these grid points was merged into the interface when taking the limit as h goes to zero, so the grid has $m = 2$ mesh cells of the same size, with only $m - 1 = 1$ grid point in the middle left. The same also happens for other values of m, there are m mesh cells, but only $m - 1$ grid points separating them in the outer grid.

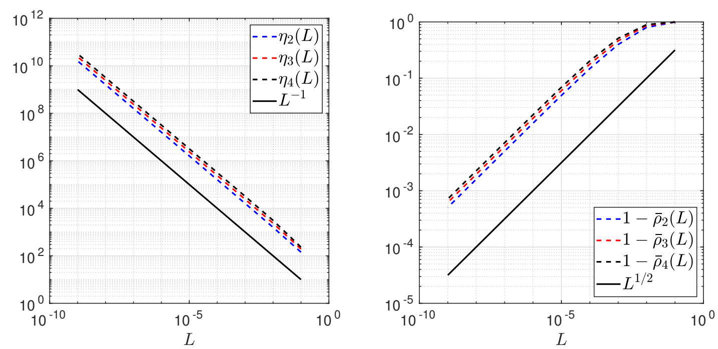

Fig. 3.3: Left: $\eta_m(L)$ versus L for $m = 2, 3, 4$. Right: $1 - \bar{\rho}_m(L)$ versus L for $m = 2, 3, 4$ (uniformly distributed) coarse points.

the analysis for uniform coarse grids with $m = 3$ and $m = 4$ points. For $m = 3$, we find the analog of (3.28) with $E_2(\tilde{h})$ replaced by

$$E_3(\tilde{h}) = \frac{2(\eta^2\tilde{h}^4 + 4\eta\tilde{h}^2 + 3)\tilde{h}}{h^2(\eta^3h^2\tilde{h}^5 + \eta^3h\tilde{h}^6 + 4\eta^2h^2\tilde{h}^3 + 6\eta^2h\tilde{h}^4 + 2\eta^2\tilde{h}^5 + 3\eta h^2\tilde{h} + 9\eta h\tilde{h}^2 + 8\eta\tilde{h}^3 + 2h + 6\tilde{h})},$$

and for the corresponding optimized parameters when h goes to zero the analog of (3.29) with the rational function $R_2(\tilde{L})$ replaced by

$$R_3(\tilde{L}) = \frac{\tilde{L}^6\eta^3 + 54\tilde{L}^4\eta^2 + 729\tilde{L}^2\eta + 1458}{6\tilde{L}^5\eta^2 + 216\tilde{L}^3\eta + 1458\tilde{L}}.$$

In Figure 3.1 (red lines) we show the Robin parameters of the BJM with $m = 3$ coarse points as a function of η and we compare it to the optimal Robin parameters of the OSM. We observe that they are closer compared to the $m = 2$ point case. This seems to suggest an improvement of the convergence factor, but the plots of the convergence factor in Figure 3.2 show that this improvement is only minor compared to the case of $m = 2$ coarse mesh points. This is also confirmed by the results in Figure 3.3 (right): we see that $\bar{\rho}_3 = 1 - O(L^{\frac{1}{2}})$, similar to the $m = 2$ coarse point case. The same happens for the $m = 4$ coarse mesh point case, where

$$R_4(\tilde{L}) = \frac{\tilde{L}^8\,\eta^4 + 128\tilde{L}^6\,\eta^3 + 5120\tilde{L}^4\,\eta^2 + 65536\tilde{L}^2\eta + 131072}{8\tilde{L}^7\,\eta^3 + 768\tilde{L}^5\,\eta^2 + 20480\tilde{L}^3\eta + 131072\tilde{L}}$$

and we show the corresponding contraction factor in Figures 3.2 (black lines) and 3.3 (right). Again we see that $\bar{\rho}_4(L) = 1 - O(L^{1/2})$.

We thus conclude that the convergence factor of the BJM with a uniform coarse grid always behaves as $1 - O(L^{\frac{1}{2}})$ independently of the number of coarse points of the grids. This shows that the OSM has a better convergence factor compared to the BJM with uniform coarse grids since its convergence factor behaves as $1 - O(L^{\frac{1}{3}})$, but BJM with uniform coarse grids converges better than classical Schwarz, which has a convergence factor $1 - O(L)$, see [11]. Is the uniformity of the coarse grids the limiting factor for BJM? We address this in the next section.

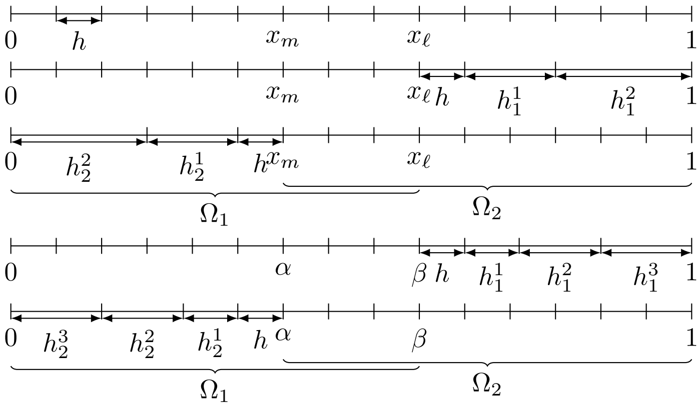

Fig. 3.4: First top row: global uniform grid. Second and third rows: stretched coarse grids with 2 points. Fourth and fifth rows: stretched coarse grids with 3 points.

3.4. Stretched coarse grid. We now consider stretched coarse grids, and start with $m = 2$ non-uniformly distributed coarse points with grid sizes h_1^1, h_1^2, h_2^1, and h_2^2, see Figure 3.4 (second and third rows). Using the finite-difference method, we discretize our problem and obtain the two linear systems $A_{\Omega_1}\boldsymbol{v} = T_2\boldsymbol{f}$ and $A_{\Omega_2}\boldsymbol{w} = T_1\boldsymbol{f}$, where A_{Ω_1} and A_{Ω_2} have the block-structures given in (2.3) with the blocks corresponding to the coarse parts of the grids that are

$$\widetilde{A}_1 = \begin{bmatrix} \frac{2}{h_2^1 h_2^2} + \eta & \frac{-2}{h_2^1(h_2^1+h_2^2)} \\ \frac{-2}{h_2^1(h+h_2^1)} & \frac{2}{hh_2^1} + \eta \end{bmatrix}, \quad \widetilde{B}_1 = \begin{bmatrix} 0 & 0 \\ \frac{-2}{h(h+h_2^1)} & 0 \end{bmatrix}, \quad C_1 = \begin{bmatrix} 0 & \frac{-1}{h^2} \\ 0 & 0 \end{bmatrix},$$
$$\widetilde{A}_2 = \begin{bmatrix} \frac{2}{hh_1^1} + \eta & \frac{-2}{h_1^1(h+h_1^1)} \\ \frac{-2}{h_1^1(h_1^1+h_1^2)} & \frac{2}{h_1^1 h_1^2} + \eta \end{bmatrix}, \quad \widetilde{B}_2 = \begin{bmatrix} 0 & \frac{-2}{h(h+h_1^1)} \\ 0 & 0 \end{bmatrix}, \quad C_2 = \begin{bmatrix} 0 & 0 \\ \frac{-1}{h^2} & 0 \end{bmatrix}.$$

Proceeding as in Section 3.3 we find after some calculations discrete BJM parameters of the form (3.28), but with $E_2(\tilde{h})$ replaced by

$$\tilde{E}_2(\tilde{h}^1, \tilde{h}^2) = \frac{2(\eta\tilde{h}^1\tilde{h}^2 + 2)(\tilde{h}^1 + \tilde{h}^2)}{D_2(\eta, h, \tilde{h}^1, \tilde{h}^2)}$$

with

$$D_2(\eta, h, \tilde{h}^1, \tilde{h}^2) = h^3\tilde{h}^1\tilde{h}^2(\tilde{h}^1 + \tilde{h}^2)(\tilde{h}^1 + h)\eta^2 + 2h^2(\tilde{h}^1 + \tilde{h}^2)(h + \tilde{h}^1)(h + \tilde{h}^2)\eta + 4h^2(h + \tilde{h}^1 + \tilde{h}^2).$$

We now use the relations $h_1^2 = 1 - \beta - h_1^1 - h$ and $h_2^2 = \alpha - h_2^1 - h$, and take the limit for $h \to 0$ to get the continuous Robin parameters of the BJM (3.29) with the rational function $R_2(\tilde{L})$ replaced by

$$\tilde{R}_2(\tilde{L}, \tilde{h}^1) := \frac{\tilde{L}(\tilde{h}^1)^2(\tilde{L} - \tilde{h}^1)\eta^2 + 2\tilde{L}^2\eta + 4}{2\tilde{L}\tilde{h}^1(\tilde{L} - \tilde{h}^1)\eta + 4\tilde{L}}, \tag{3.30}$$

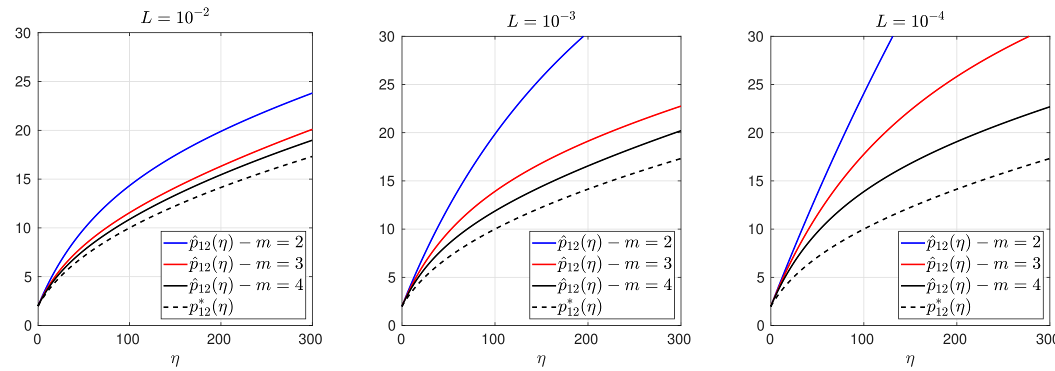

Fig. 3.5: Comparison of the Robin parameters p^*_{12} of the OSM and $\hat{p}_{12}$ of the BJM for $m = 2, 3, 4$ stretched (optimized) coarse points and overlap $L = 10^{-2}$ (left), $L = 10^{-3}$ (middle), $L = 10^{-4}$ (right).

which shows that the coefficients in the rational function in η can now be controlled by the mesh parameter $\tilde{h}^1$! To understand the impact of this new degree of freedom from the coarse mesh, we assume for simplicity that $\alpha = \frac{1-L}{2}$ and $\beta = \frac{1+L}{2}$, and $h_1^1 = h_2^1$ and $h_1^2 = h_2^2$. Inserting $\hat{p}_{12}$ and $\hat{p}_{21}$ into (3.5) and minimizing the maximum of the resulting convergence factor (3.5) over all frequencies η (using the MATLAB function `fminunc`), we find the best choice for the mesh stretching $h_1^{1\star}(L)$ that makes the convergence factor as small as possible. We show in Figure 3.5 the behavior of the Robin parameter $\hat{p}_{12}(\eta)$ (blue lines) compared to the OSM parameter $p^\star_{12}(\eta)$ (black dashed lines) for different overlaps L. Clearly, the curves are very different from the ones corresponding to the uniform mesh (Figure 3.1) which are very stable with respect to the overlap L. In the stretched case, the coarse mesh is strongly influenced by the overlap: the smaller the overlap, the more work needs/can be done in the optimization of the coarse points. The corresponding convergence factors are shown in Figure 3.6 (blue lines), where one can now observe how they have two maxima. Hence, the optimization of the coarse points is solved when an equioscillation of the two maxima is obtained. If one compares these plots to the ones presented in Figure 3.2, the enormous improvement obtained by optimizing the position of the $m = 2$ coarse points is clearly visible. This behavior is even more evident if one compares the deterioration of $\bar{\rho}_2$ of Figure 3.3 (right) with the corresponding one of Figure 3.7 (right - blue line): we observe that now the deterioration of the contraction factors with respect of the overlap is $\bar{\rho}_2(L) = 1 - O(L^{\frac{1}{4}})$. In Figure 3.7 (left - blue line) we show the dependence of the optimized mesh position $h_1^{1\star}$ on L. We observe that

$$h_1^{1\star} = O(L^{\frac{1}{2}}) \quad \text{for } m = 2. \tag{3.31}$$

Finally, in Figure 3.8 (left) we show the dependence of the frequencies η_1 and η_2 (the maximum points) on L and we observe that

$$\eta_1 = O(L^{-\frac{1}{2}}), \quad \eta_2 = O(L^{-\frac{3}{2}}) \quad \text{for } m = 2. \tag{3.32}$$

We prove these numerical observations in the next theorem.

Theorem 3.6 (Optimized stretched grid for $m = 2$). *The Bank-Jimack Algorithm 2.1 with partition of unity (2.9), overlap L, and two equal subdomains $\alpha = \frac{1-L}{2}$ and $\beta = \frac{1+L}{2}$ has for $m = 2$*

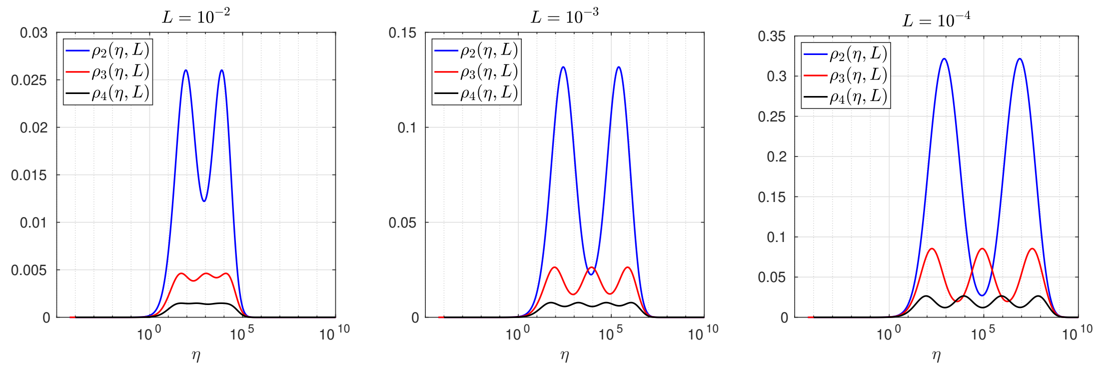

Fig. 3.6: Convergence factors $\rho_m(\eta, L)$ as functions of η for $m = 2, 3, 4$ stretched (optimized) coarse points and $L = 10^{-2}$ (left), $L = 10^{-3}$ (middle), $L = 10^{-4}$ (right). Notice the different scales of the three plots.

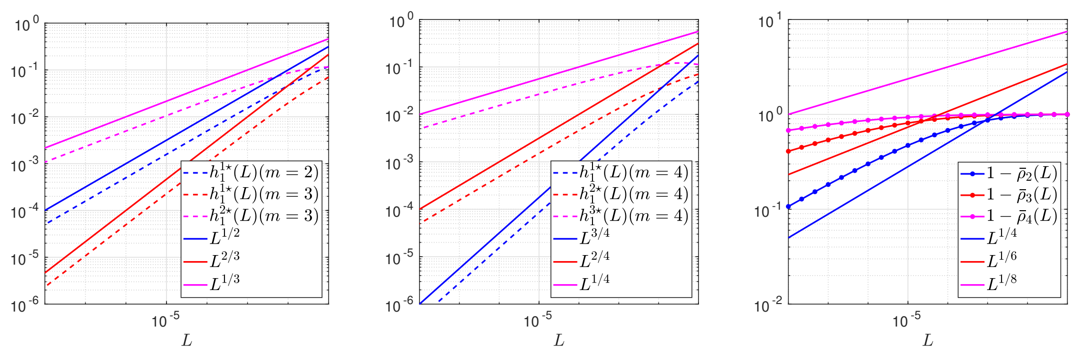

Fig. 3.7: Left: $h^{j\star}(L)$ versus L for $m = 2, 3$. Middle: $h^{j\star}(L)$ versus L for $m = 4$. Right: $1 - \bar{\rho}_m(L)$ versus L for $m = 2, 3, 4$ stretched (optimized) coarse points.

and overlap L small the optimized stretched grid points and associated contraction factor

$$h_1^{1\star} = h_2^{1\star} = \frac{1}{2}\sqrt{L}, \quad \bar{\rho}_2(L) = 1 - 8\sqrt{2}L^{\frac{1}{4}} + O(\sqrt{L}). \tag{3.33}$$

Proof. The system of equations satisfied when the maxima of $\rho_2(\eta, L)$ equioscillate as shown at the optimum in Figure 3.2 is

$$\rho_2(\eta_1, L) = \rho_2(\eta_2, L), \quad \partial_\eta \rho_2(\eta_1, L) = 0, \quad \partial_\eta \rho_2(\eta_2, L) = 0. \tag{3.34}$$

To solve this non-linear system asymptotically, we insert the ansatz $h_1^{1\star} = h_2^{1\star} := C_{h^1}\sqrt{L}$ and $\eta_1 := C_{\eta_1} L^{-\frac{1}{2}}$ and $\eta_2 := C_{\eta_2} L^{-\frac{3}{2}}$ into the system (3.34), expand for overlap L small and find the relations

$$\frac{2(C_{\eta_1}C_{h^1} + 4)}{\sqrt{C_{\eta_1}}} = \frac{C_{\eta_2}C_{h^1} + 4}{\sqrt{C_{\eta_2}}C_{h^1}}, \quad C_{\eta_1}C_{h^1} = 4, \quad C_{\eta_2}C_{h^1} = 4.$$

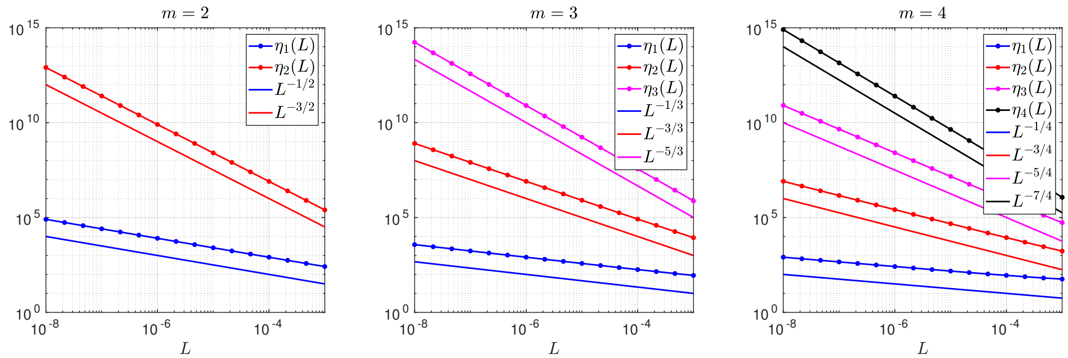

Fig. 3.8: Maximum points $\eta_j(L)$ for $m = 2$ (left), $m = 3$ (middle) and $m = 4$ (right).

The solution is $C_{\eta_1} = C_{\eta_2} = 8$ and $C_{h^1} = \frac{1}{2}$, which leads when inserted with the ansatz into $\rho_2(\eta_1, L)$ to (3.33) after a further expansion for L small. ∎

We thus conclude that the convergence factor of the BJM with an optimized stretched coarse mesh with $m = 2$ points behaves better than the convergence factor of the OSM with Robin transmission conditions which is $\rho_{OSM} = 1 - O(L^{\frac{1}{3}})$, but worse than OSM with second order (Ventcell) transmission conditions, which is $\rho_{OSM} = 1 - O(L^{\frac{1}{5}})$; see [11].

Let us now consider the case of $m = 3$ non-uniformly distributed coarse points with sizes h_1^1, h_1^2, and h_1^3, see Figure 3.4 (fourth and fifth rows). Notice also the geometric relations $h_2^3 = \alpha - (h + h_2^1 + h_2^2)$ and $h_1^3 = 1 - \beta - (h + h_1^1 + h_1^2)$. Similar calculations as before (see also [18]) lead after expanding for h going to zero to the continuous Robin parameters of the BJM (3.29) with the rational function $R_2(\tilde{L})$ replaced by

(3.35)
$$\tilde{R}_3(\tilde{L}, \tilde{h}^1, \tilde{h}^2) := \frac{(\tilde{h}^1)^2\tilde{h}^2(\tilde{h}^1+\tilde{h}^2)(\tilde{L}-\tilde{h}^1)(\tilde{L}-\tilde{h}^1-\tilde{h}^2)\eta^3+2(\tilde{h}^1+\tilde{h}^2)(\tilde{L}-\tilde{h}^1)(\tilde{L}\tilde{h}^1+\tilde{L}\tilde{h}^2-2\tilde{h}^1\tilde{h}^2-(\tilde{h}^2)^2)\eta^2+4\tilde{L}^2\eta+8}{2\tilde{h}^1\tilde{h}^2(\tilde{h}^1+\tilde{h}^2)(\tilde{L}-\tilde{h}^1)(\tilde{L}-\tilde{h}^1-\tilde{h}^2)\eta^2+4(\tilde{h}^1+\tilde{h}^2)(\tilde{L}-\tilde{h}^2)(\tilde{L}-\tilde{h}^1)\eta+8\tilde{L}}.$$

We thus have now two parameters from the stretched mesh from each side to optimize the convergence factor! We set again $\alpha = \frac{1-L}{2}$ and $\beta = \frac{1+L}{2}$, and $h_1^j = h_2^j$, $j = 1, 2, 3$, and inserting $\hat{p}_{12}$ and $\hat{p}_{21}$ into the convergence factor (3.5) and minimizing the maximum of the resulting convergence factor over all frequencies η, we find the best choice for the mesh stretching $h_1^{1\star}(L)$, $h_1^{2\star}(L)$ that makes the convergence factor as small as possible, shown in Figure 3.6 for a typical example in red. We notice that now three local maxima are present and equioscillate. In Figure 3.7 (left), we show how the optimized choice of the stretched mesh parameters $h_1^{1\star}(L)$, $h_1^{2\star}(L)$ decay when the overlap L becomes small, and observe that

$$h_1^{1\star} = O(L^{\frac{2}{3}}), \quad h_1^{2\star} = O(L^{\frac{1}{3}}) \quad \text{for } m = 3.$$

Similarly, in Figure 3.8 (middle) we find for the maximum points η_1, η_2, and η_3 the asymptotic behavior

$$\eta_1 = O(L^{-\frac{1}{3}}), \quad \eta_2 = O(L^{-\frac{3}{3}}), \quad \eta_3 = O(L^{-\frac{5}{3}}) \quad \text{for } m = 3.$$

THEOREM 3.7 (Optimized stretched grid for $m = 3$). *Under the same assumptions as in Theorem 3.6, the Bank Jimack Algorithm 2.1 has for $m = 3$ and overlap L small the optimized stretched grid points and associated contraction factor*

$$h_1^{1\star} = h_2^{1\star} = \frac{1}{2}L^{\frac{2}{3}}, \quad h_1^{2\star} = h_2^{2\star} = \frac{1}{2}L^{\frac{1}{3}}, \quad \bar{\rho}_3(L) = 1 - 8\sqrt{2}L^{\frac{1}{6}} + O(L^{\frac{1}{3}}). \tag{3.36}$$

Proof. The system of equations satisfied when the maxima of $\rho_2(\eta, L)$ equioscillate as shown at the optimum in Figure 3.2 is

$$\rho_2(\eta_1, L) = \rho_2(\eta_2, L),\ \rho_2(\eta_2, L) = \rho_2(\eta_3, L),\ \partial_\eta \rho_2(\eta_1, L) = 0,\ \partial_\eta \rho_2(\eta_2, L) = 0,\ \partial_\eta \rho_2(\eta_3, L) = 0. \tag{3.37}$$

Inserting the ansatz $h_1^{1\star} = h_2^{1\star} := C_{h^1} L^{\frac{2}{3}}$, $h_1^{2\star} = h_2^{2\star} := C_{h^2} L^{\frac{1}{3}}$, and $\eta_1 := C_{\eta_1} L^{-\frac{1}{3}}$, $\eta_2 := C_{\eta_2} L^{-\frac{3}{3}}$, $\eta_2 := C_{\eta_2} L^{-\frac{5}{3}}$ into the system (3.37), we can solve the system asymptotically for the constants when the overlap L becomes small, which leads to (3.36). ∎

The analysis for $m = 4$ stretched coarse points follows the same lines, and we find after a longer computation for the continuous Robin parameters of the BJM (3.29) with the rational function $R_2(\tilde{L})$ replaced by (see also [18] for details)

$$\tilde{R}_4(\tilde{L}, \tilde{h}^1, \tilde{h}^2, \tilde{h}^3) = \frac{\tilde{N}_4(\tilde{L}, \tilde{h}^1, \tilde{h}^2, \tilde{h}^3)}{\tilde{D}_4(\tilde{L}, \tilde{h}^1, \tilde{h}^2, \tilde{h}^3)} \tag{3.38}$$

with the numerator and denominator given by

$$\begin{aligned}
\tilde{N}_4 = {} & (\tilde{h}^1)^2 \tilde{h}^2 \tilde{h}^3 (\tilde{h}^3 + \tilde{h}^2)(\tilde{h}^2 + \tilde{h}^1)(\tilde{L} - \tilde{h}^1 - \tilde{h}^2)(\tilde{L} - \tilde{h}^1 - \tilde{h}^2 - \tilde{h}^3)\eta^4 \\
& + 2(\tilde{L} - \tilde{h}^1 - \tilde{h}^2)(\tilde{h}^3 + \tilde{h}^2)(\tilde{h}^2 + \tilde{h}^1)\big((\tilde{L} - 2\tilde{h}^3)(\tilde{h}^1)^2 - (\tilde{h}^1)^3 + \tilde{h}^3(\tilde{L} - 2\tilde{h}^2 - \tilde{h}^3)\tilde{h}^1 + \tilde{h}^3\tilde{h}^2(\tilde{L} - \tilde{h}^2 - \tilde{h}^3)\big)\eta^3 \\
& + \big((8\tilde{h}^2 + 8\tilde{h}^3 - 4\tilde{L})(\tilde{h}^1)^3 + 4(\tilde{L} - \tilde{h}^2 - \tilde{h}^3)(\tilde{L} - 3\tilde{h}^2 - 3\tilde{h}^3)(\tilde{h}^1)^2 + 8(\tilde{h}^3 + \tilde{h}^2)((\tilde{h}^2)^2/2 + ((5\tilde{h}^3)/2 - 2\tilde{L})\tilde{h}^2 \\
& \quad + \tilde{L}^2 - 2\tilde{L}\tilde{h}^3 + (\tilde{h}^3)^2/2)\tilde{h}^1 + 4((\tilde{L} - 2\tilde{h}^3)\tilde{h}^2 + \tilde{h}^3(\tilde{L} - \tilde{h}^3))(\tilde{h}^3 + \tilde{h}^2)(\tilde{L} - \tilde{h}^2)\big)\eta^2 + 8\tilde{L}^2\eta + 16, \\
\tilde{D}_4 = {} & 2\tilde{h}^1 \tilde{h}^2 \tilde{h}^3 (\tilde{h}^3 + \tilde{h}^2)(\tilde{h}^2 + \tilde{h}^1)(\tilde{L} - \tilde{h}^1 - \tilde{h}^2)(\tilde{L} - \tilde{h}^1 - \tilde{h}^2 - \tilde{h}^3)\eta^3 \\
& + 4(\tilde{L} - \tilde{h}^1 - \tilde{h}^2)(\tilde{h}^3 + \tilde{h}^2)(\tilde{h}^2 + \tilde{h}^1)\big((\tilde{L} - 2\tilde{h}^3)\tilde{h}^1 - (\tilde{h}^1)^2 + \tilde{h}^3(\tilde{L} - \tilde{h}^2 - \tilde{h}^3)\big)\eta^2 \\
& + \big((8\tilde{h}^2 + 8\tilde{h}^3 - 8\tilde{L})(\tilde{h}^1)^2 + 8(\tilde{L} - \tilde{h}^2 - \tilde{h}^3)^2\tilde{h}^1 + 8(\tilde{h}^3 + \tilde{h}^2)(\tilde{L} - \tilde{h}^3)(\tilde{L} - \tilde{h}^2)\big)\eta + 16\tilde{L},
\end{aligned}$$

which leads to the results shown in Figures 3.6, 3.7 (middle), 3.8 (right), which show that

$$h_1^{1\star} = O(L^{\frac{3}{4}}), \quad h_1^{2\star} = O(L^{\frac{2}{4}}), \quad h_1^{3\star} = O(L^{\frac{1}{4}}) \quad \text{for } m = 4,$$

and for the maximum points we find

$$\eta_1 = O(L^{-\frac{1}{4}}), \quad \eta_2 = O(L^{-\frac{3}{4}}), \quad \eta_3 = O(L^{-\frac{5}{4}}), \quad \eta_4 = O(L^{-\frac{7}{4}}) \quad \text{for } m = 4. \tag{3.39}$$

THEOREM 3.8 (Optimized stretched grid for $m = 4$). *Under the same assumptions of Theorem 3.6, the Bank-Jimack Algorithm 2.1 has for $m = 4$ and overlap L small the optimized stretched grid points and associated contraction factor*

$$h_1^{1\star} = h_2^{1\star} = \frac{1}{2}L^{\frac{3}{4}},\ h_1^{2\star} = h_2^{2\star} = \frac{1}{2}L^{\frac{2}{4}},\ h_1^{3\star} = h_2^{3\star} = \frac{1}{2}L^{\frac{1}{4}},\ \bar{\rho}_4(L) = 1 - 8\sqrt{2}L^{\frac{1}{8}} + O(L^{\frac{1}{4}}). \tag{3.40}$$

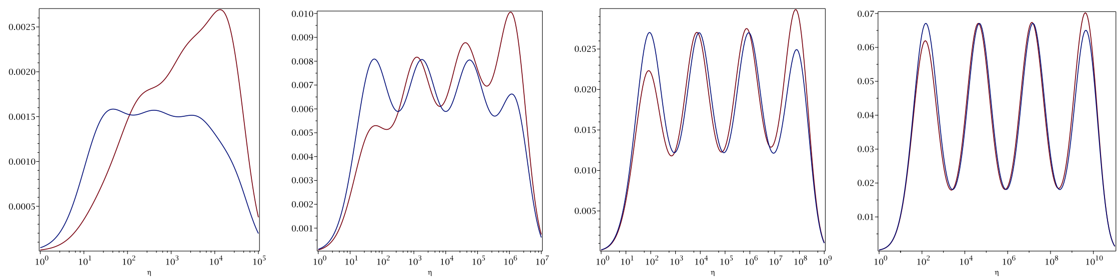

Fig. 3.9: Asymptotic stretching from Conjecture 3.9 (red) compared to the direct geometric stretching in (3.43) (blue) for overlap sizes $L = \frac{1}{10^j}$, $j = 2, 3, 4, 5$.

Proof. We proceed as in the proof of Theorem 3.6 and 3.7. ∎

These results for optimized stretched coarse grids with $m = 2$, $m = 3$, and $m = 4$ points lead us to formulate the following conjecture:

Conjecture 3.9. *The Bank-Jimack Algorithm 2.1 with partition of unity (2.9), overlap L, and two equal subdomains $\alpha = \frac{1-L}{2}$ and $\beta = \frac{1+L}{2}$, has for overlap L small the optimized stretched grid point locations and associated contraction factor*

$$h_1^{j\star} = h_2^{j\star} \sim \frac{1}{2} L^{\frac{m-j}{m}}, \; j = 1, 2, \ldots, m-1, \quad \bar{\rho}_m(L) \sim 1 - 8\sqrt{2} L^{\frac{1}{2m}}. \tag{3.41}$$

This result shows that one should choose a geometric coarsening related to the overlap to form the outer coarse grid leading to the best performance for the Bank-Jimack domain decomposition algorithm. A practical approach is to just take a geometrically stretched grid with respect to the overlap size,

$$h_j := L^{\frac{m-1}{m}}, \quad j = 1, \ldots, m, \tag{3.42}$$

and then to sum the step sizes h_j and scale the result to the size of the outer remaining domain, say $\hat{L}$, to get the actual mesh sizes $\tilde{h}_j$ to use,

$$s := \sum_{j=1}^{m} h_j = \frac{1-L}{1-L^{\frac{1}{m}}} \quad \Longrightarrow \quad \tilde{h}_j := \frac{h_j}{s} \hat{L} = \frac{L^{-\frac{j}{m}} - L^{\frac{1-j}{m}}}{L^{-1} - 1} \hat{L}. \tag{3.43}$$

This direct geometric stretching including the last grid cell is preasymptotically even a bit better, as one can see in Figure 3.9.

4. Numerical experiments. In this section, we present numerical experiments to illustrate our theoretical results. We start with experiments for equally spaced coarse meshes, and compare their performance with the optimized geometrically stretched ones. We consider both a case of constant overlap L and a case where the overlap is proportional to the mesh size. We then also explore numerically the influence of coarsening the meshes in the direction tangential to the interface. In all these cases, we study the performance of the BJM as a stationary method and as a preconditioner for GMRES. We discretize the Poisson equation (2.6) (defined on a unit square $\Omega = (0, 1)^2$) using

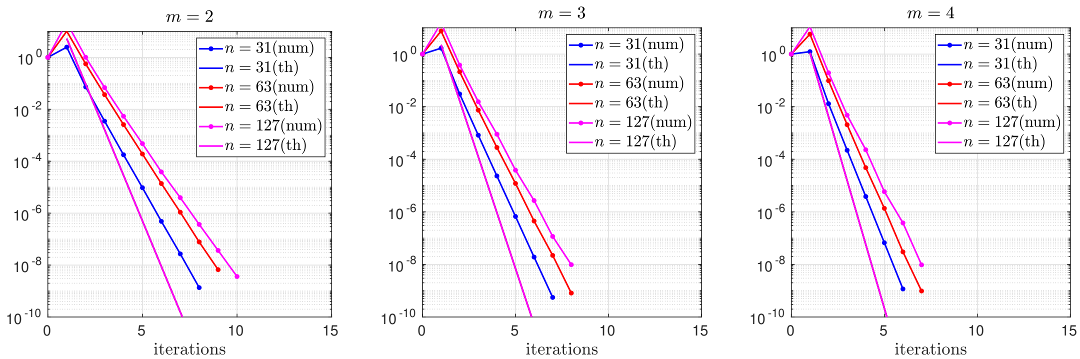

Fig. 4.1: Decay of the error of the BJM (stationary) iteration for $m = 2$ (left), $m = 3$ (middle) and $m = 4$ (right) uniformly distributed coarse points (in direction x) and constant overlap $L = \frac{1}{16}$. Notice that, in each plot, the solid curves representing the theoretical convergence estimates coincide since they correspond to the same overlap L.

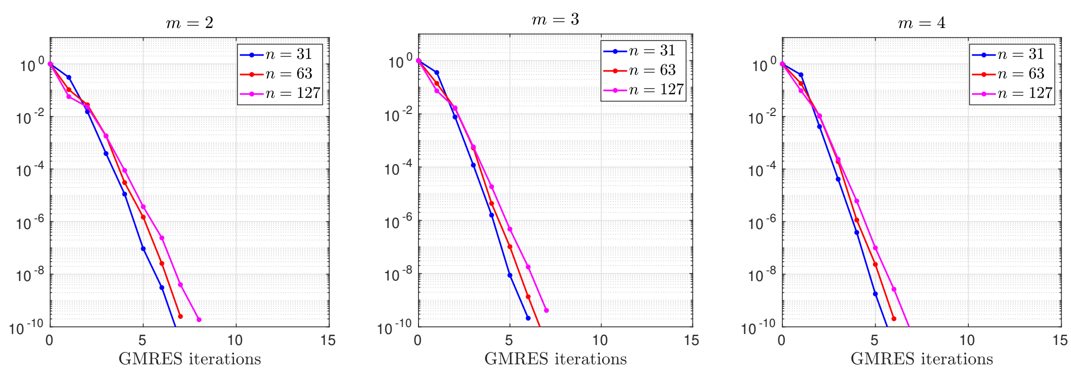

Fig. 4.2: Decay of the residual of the GMRES iteration preconditioned by BJM for $m = 2$ (left), $m = 3$ (middle) and $m = 4$ (right) uniformly distributed coarse points (in direction x) and constant overlap $L = \frac{1}{16}$.

n^2 (interior) mesh points where $n = 2^\ell - 1$, for $\ell = 5, 6, 7$, is the number of interior points on the global fine mesh in each direction (Figure 2.1). The results corresponding to a uniform coarsening in direction x are presented in Section 4.1. Section 4.2 focuses on optimized stretched coarsening in direction x. Finally, in Section 4.3 we study the effect of the coarsening in both directions x and y.

4.1. Uniform coarsening in direction x. We start with the equally spaced coarse mesh case, coarsened only along the x axis. At first, we consider the case with a constant overlap $L = \frac{1}{16}$, which corresponds to $n_s = 3, 5, 9$ for $\ell = 5, 6, 7$, respectively. Moreover, to test the methods in the cases studied by our theoretical analysis, we consider $m = 2, 3, 4$ coarse mesh points. The results of the numerical experiments are shown in Figure 4.1 and Figure 4.2. The former shows the decay

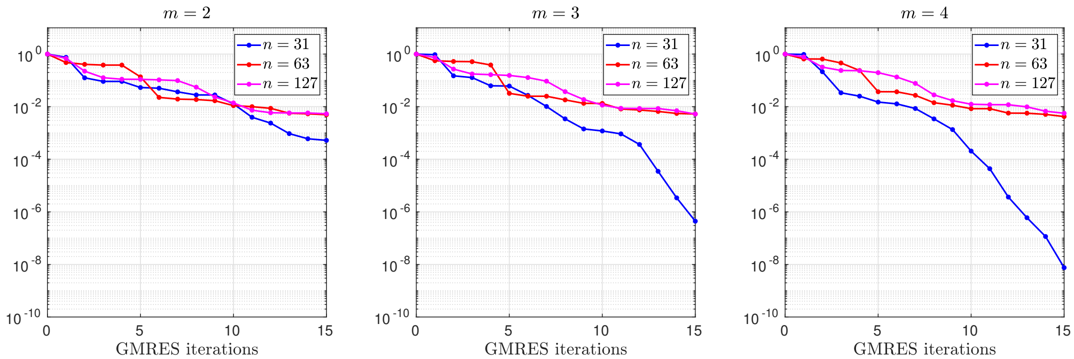

Fig. 4.3: Decay of the residual of the GMRES iteration preconditioned by BJM with the original partition of unity used in [1] for $m = 2$ (left), $m = 3$ (middle) and $m = 4$ (right) uniformly distributed coarse points (in direction x) and constant overlap $L = \frac{1}{16}$.

of the error corresponding to the BJM as a stationary iteration, while the latter presents the decay of the GMRES residuals along the iterations. All the plots show that the effect of the number of coarse points on the convergence is very mild. This corresponds to the results discussed in Section 3.3 and shown in Figure 3.3 (right): if the overlap L is constant, the contraction factor does not improve significantly if more (uniformly distributed) coarse points are considered. The same effect can be observed in the GMRES convergence.

Now, we wish to study the effect of the new partition of unity proposed in [7] and constructed using (2.4). This was used in all the experiments discussed above. If we use the original partition of unity, we already know from [7] that the BJM does not converge as a stationary method. Therefore, we use it only as a preconditioner for GMRES and obtain the results depicted in Figure 4.3. By comparing the results of this figure with the ones of Figure 4.2, we see that the effect of the new partition of unity is tremendous: GMRES converges much faster and is very robust against mesh refinements. For further information on the influence of the partition of unity on Schwarz methods, see [13].

Now, let us now consider an overlap proportional to the mesh size, namely $L = 2h$, and repeat the experiments already described. The corresponding results are shown in Figures 4.4, 4.5 and 4.6. As before, we observe that the BJM method (as stationary iteration and as preconditioner) is robust against the number of coarse mesh points. In this case, the convergence deteriorates with mesh refinement since the overlap L gets smaller proportionally to h. Finally, we observe again the great impact of the new partition of unity by comparing Figures 4.5 and 4.6.

4.2. Stretched coarsening in direction x. In this section, we repeat the experiments presented in Section 4.1, but we optimize the position of the coarse mesh points by minimizing numerically the contraction factor (as in Section 3.4). We begin with the case of constant overlap $L = \frac{1}{16}$. The corresponding numerical results are shown in Figures 4.7 and 4.8. These results show that optimizing the coarse mesh leads to a faster method which is robust against the mesh refinement. However, due to the constant overlap, there is only little improvement with respect to the constant coarsening case. To better appreciate the effect of the mesh optimization, we consider the case with overlap $L = 2h$. The corresponding results are shown in Figures 4.9 and 4.10. By comparing

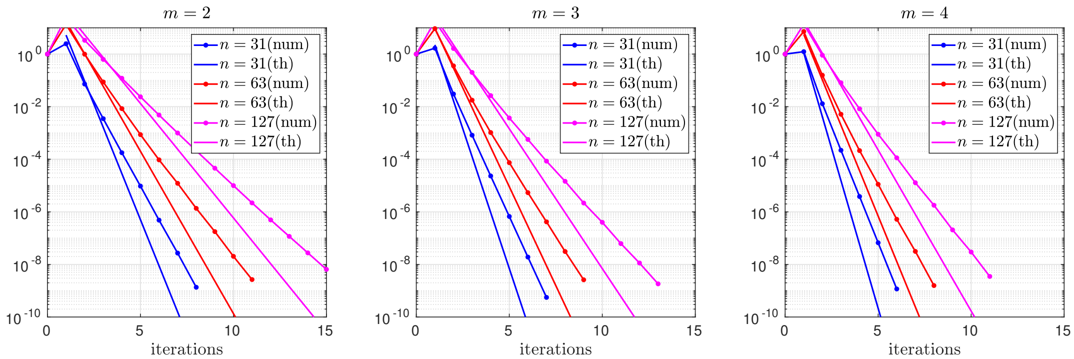

Fig. 4.4: Decay of the error of the BJM (stationary) iteration for $m = 2$ (left), $m = 3$ (middle) and $m = 4$ (right) uniformly distributed coarse points (in direction x) and overlap $L = 2h$.

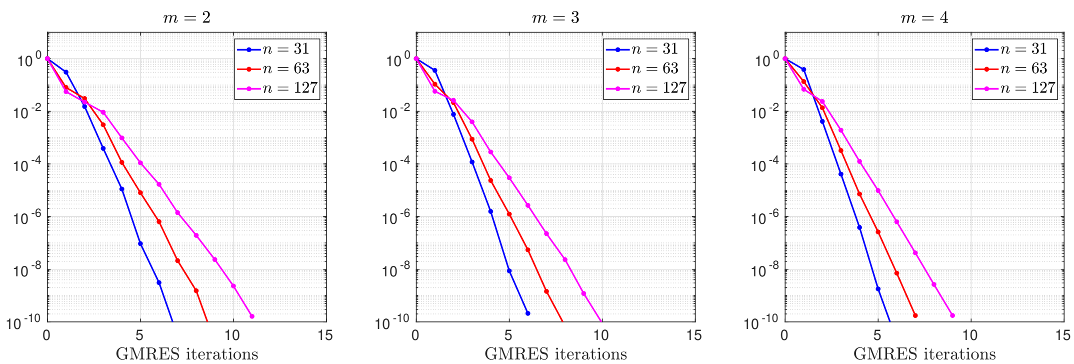

Fig. 4.5: Decay of the residual of the GMRES iteration preconditioned by BJM and for $m = 2$ (left), $m = 3$ (middle) and $m = 4$ (right) uniformly distributed coarse points (in direction x) and overlap $L = 2h$.

these results with the ones of Figures 4.4 and 4.5, one can see clearly the improvement of the BJM convergence: the number of iterations (for both stationary and preconditioned GMRES methods) are essentially halved in the case of finer meshes.

4.3. Coarsening in direction x and y. We conclude our numerical experiments by studying the effect of a (uniform) coarsening in both x and y directions. As before, we consider both cases $L = \frac{1}{16}$ and $L = 2h$. The results shown in Figures 4.11, 4.12, 4.13 and 4.14 indicate that a coarsening in direction y does not have a significant impact on the convergence of the BJM method.

5. Conclusions. We provided a detailed convergence analysis of the Bank-Jimack domain decomposition method for the Laplace problem and two subdomains. Our analysis reveals that one should coarsen the outer mesh each subdomain uses in a geometric progression related to the size of the overlap if one wants to get good convergence, and arbitrarily weak dependence on the overlap size is possible (see also [14] for a different technique reaching this). In order for these results to

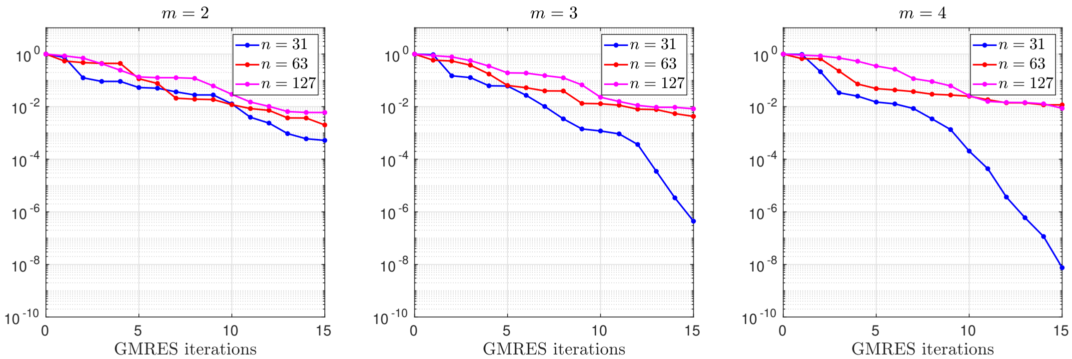

Fig. 4.6: Decay of the residual of the GMRES iteration preconditioned by BJM with the original partition of unity used in [1] for $m = 2$ (left), $m = 3$ (middle) and $m = 4$ (right) uniformly distributed coarse points (in direction x) and overlap $L = 2h$.

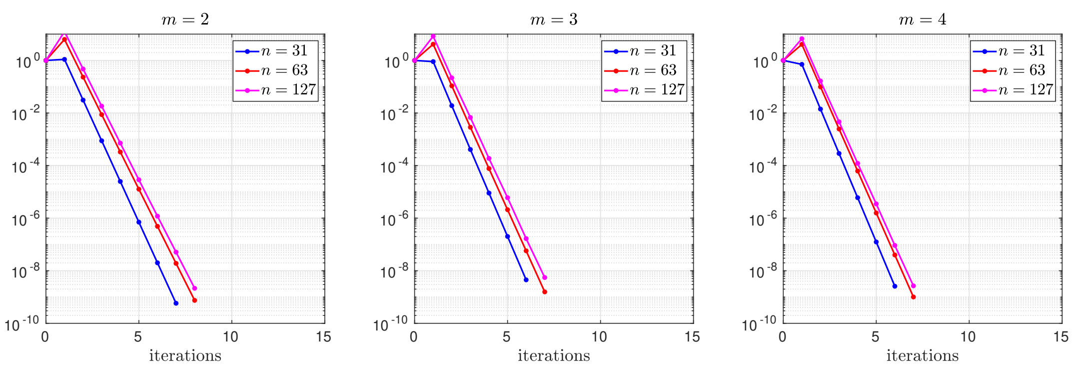

Fig. 4.7: Decay of the error of the BJM (stationary) iteration for $m = 2$ (left), $m = 3$ (middle) and $m = 4$ (right) stretched (optimized) coarse points (in direction x) and constant overlap $L = \frac{1}{16}$.

hold one has to use a slightly modified partition of unity in the Bank-Jimack algorithm, without which the convergence of the method is much worse. We obtained our results by an asymptotic process as the subdomain mesh size goes to zero, and thus the results hold at the continuous level.

A possibility for further optimization at the discrete level is the observation that the maxima in the optimized method, shown in Figure 3.6, occur for very high values of η which represent a Fourier frequency, and thus may lie outside of the frequencies representable on the mesh used. This can be seen quantitatively for example from the stretched case for $m = 4$, where the largest $\eta_4 = O(L^{-\frac{7}{4}})$, and the highest Fourier frequency can be estimated as $\eta = O(h^{-1})$, see [11]. Hence, if the overlap is of the order of the mesh size, $L = h$, η_4 would be already much larger than what the grid can represent, and we see in fact from (3.39) that only half the number of bumps would need to be taken in consideration for the optimization.

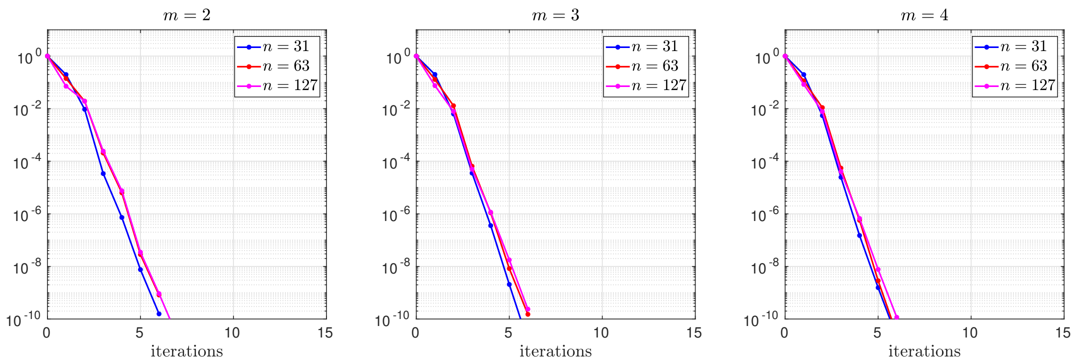

Fig. 4.8: Decay of the residual of the GMRES iteration preconditioned by BJM and for $m = 2$ (left), $m = 3$ (middle) and $m = 4$ (right) stretched (optimized) coarse points (in direction x) and constant overlap $L = \frac{1}{16}$.

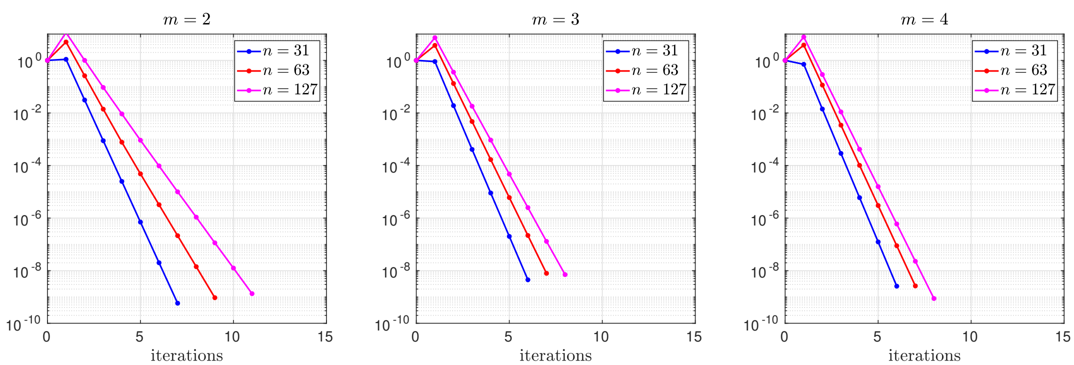

Fig. 4.9: Decay of the error of the BJM (stationary) iteration for $m = 2$ (left), $m = 3$ (middle) and $m = 4$ (right) stretched (optimized) coarse points (in direction x) and overlap $L = 2h$.

REFERENCES

[1] R. E. Bank and P. K. Jimack, *A new parallel domain decomposition method for the adaptive finite element solution of elliptic partial differential equations*, Concurrency and Computation: Practice and Experience, 13 (2001).

[2] R. E. Bank and P. S. Vassilevski, *Convergence analysis of a domain decomposition paradigm*, Computing and Visualization in Science, 11 (2008), pp. 333–350.

[3] J. F. Bourgat, R. Glowinski, P. L. Tallec, and M. Vidrascu, *Variational Formulation and Algorithm for Trace Operator in Domain Decomposition Calculations*, in Domain decomposition methods, SIAM, Philadelphia, PA, 1989, pp. 3–16.

[4] F. Chaouqui, G. Ciaramella, M. J. Gander, and T. Vanzan, *On the scalability of classical one-level domain-decomposition methods*, Vietnam Journal of Mathematics, 46(4) (2018), pp. 1053–1088.

[5] G. Ciaramella and M. J. Gander, *Analysis of the parallel Schwarz method for growing chains of fixed-sized subdomains: Part I*, SIAM J. Numer. Anal., 55 (2017), pp. 1330–1356.

[6] G. Ciaramella and M. J. Gander, *Iterative Methods and Preconditioners for Systems of Linear Equations*,

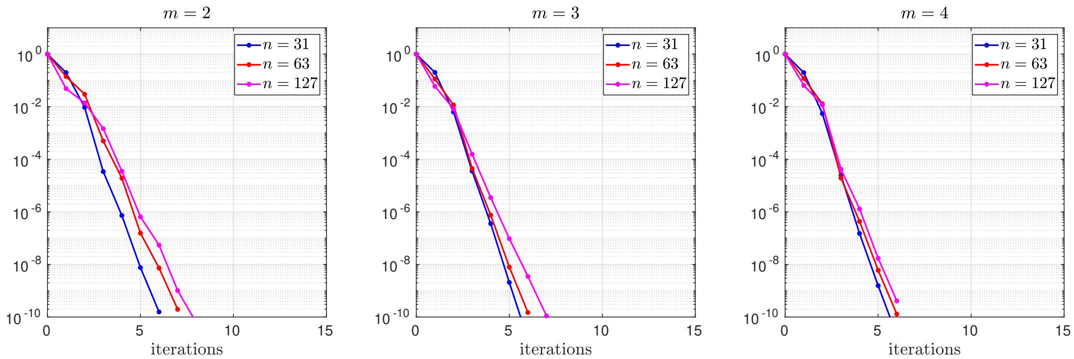

Fig. 4.10: Decay of the residual of the GMRES iteration preconditioned by BJM for $m = 2$ (left), $m = 3$ (middle) and $m = 4$ (right) stretched (optimized) coarse points (in direction x) and overlap $L = 2h$.

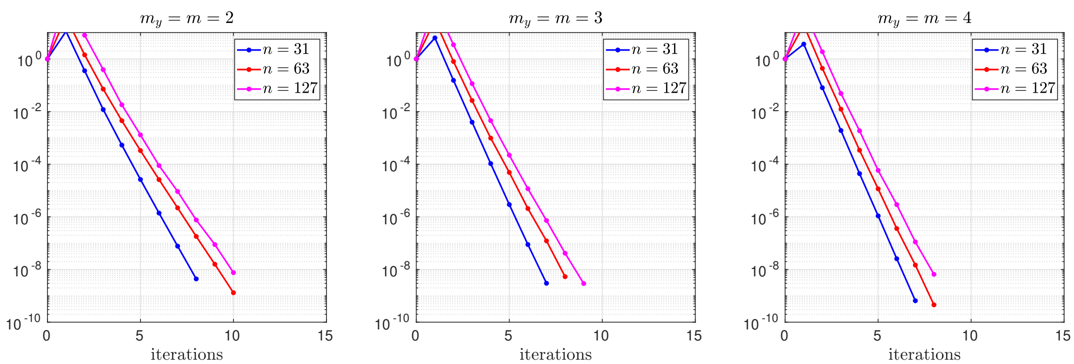

Fig. 4.11: Decay of the error of the BJM (stationary) iteration for $m_y = m = 2$ (left), $m_y = m = 3$ (middle) and $m_y = m = 4$ (right) uniformly distributed coarse points (in direction x and y) and constant overlap $L = \frac{1}{16}$.

to appear in SIAM, 2021.

[7] G. Ciaramella, M. J. Gander, and P. Mamooler, *The domain decomposition method of bank and jimack as an optimized schwarz method*, Domain Decomposition Methods in Science and Engineering XXV, LNCSE, Springer-Verlag, (2019).

[8] E. Efstathiou and M. J. Gander, *Why restricted additive Schwarz converges faster than additive Schwarz*, BIT, 43 (2003), pp. 945–959.

[9] C. Farhat, J. Mandel, and F. X. Roux, *Optimal convergence properties of the FETI domain decomposition method*, Computer methods in applied mechanics and engineering, 115 (1994), pp. 365–385.

[10] C. Farhat and F.-X. Roux, *A method of finite element tearing and interconnecting and its parallel solution algorithm*, International Journal for Numerical Methods in Engineering, 32 (1991), pp. 1205–1227.

[11] M. J. Gander, *Optimized Schwarz methods*, SIAM Journal on Numerical Analysis, 44 (2006).

[12] M. J. Gander, *Schwarz methods over the course of time*, Electron. Trans. Numer. Anal, 31 (2008), pp. 228–255.

[13] M. J. Gander, *Does the partition of unity influence the convergence of schwarz methods?*, in Domain Decomposition Methods in Science and Engineering XXV, Berlin, Heidelberg, 2020, Springer Berlin Heidelberg.

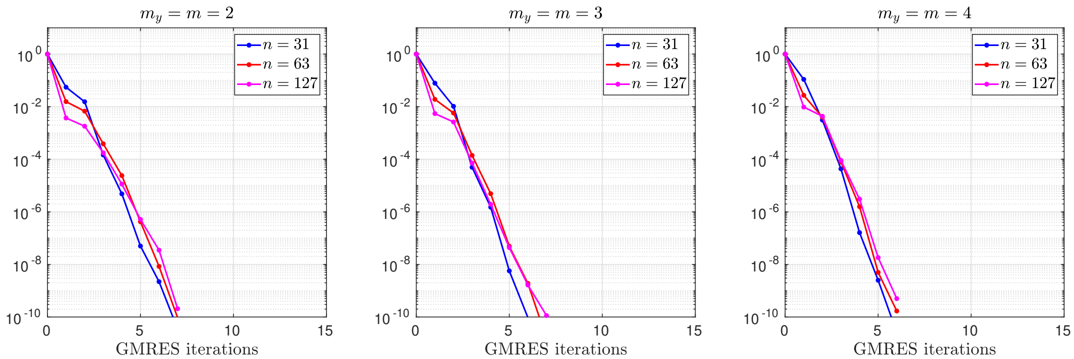

Fig. 4.12: Decay of the residual of the GMRES iteration preconditioned by BJM for $m_y = m = 2$ (left), $m_y = m = 3$ (middle) and $m_y = m = 4$ (right) uniformly distributed coarse points (in direction x and y) and constant overlap $L = \frac{1}{16}$.

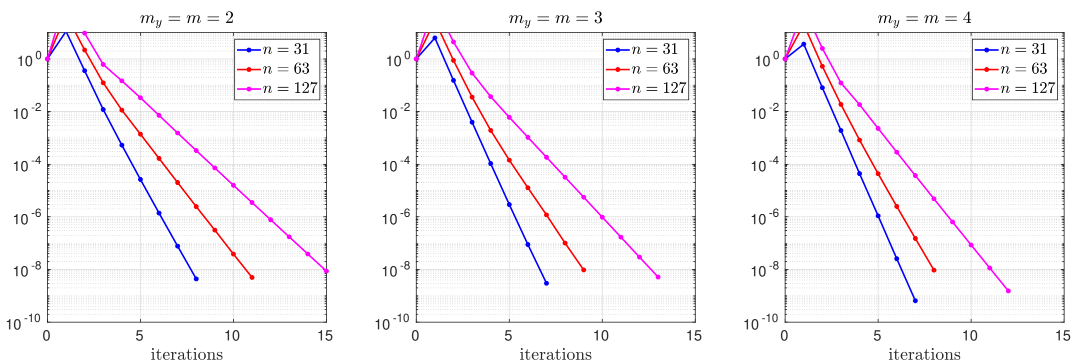

Fig. 4.13: Decay of the error of the BJM (stationary) iteration for $m_y = m = 2$ (left), $m_y = m = 3$ (middle) and $m_y = m = 4$ (right) uniformly distributed coarse points (in direction x and y) and overlap $L = 2h$.

[14] M. J. Gander and G. H. Golub, *A non-overlapping optimized Schwarz method which converges with an arbitrarily weak dependence on h*, in Fourteenth International Conference on Domain Decomposition Methods, 2002.

[15] M. J. Gander, L. Halpern, and F. Nataf, *Optimal convergence for overlapping and non-overlapping Schwarz waveform relaxation*, in Eleventh international Conference of Domain Decomposition Methods, C.-H. Lai, P. Bjørstad, M. Cross, and O. Widlund, eds., ddm.org, 1999.

[16] M. J. Gander and H. Zhang, *A class of iterative solvers for the Helmholtz equation: Factorizations, sweeping preconditioners, source transfer, single layer potentials, polarized traces, and optimized Schwarz methods*, SIAM Review, 61(1) (2019), pp. 3–76.

[17] P.-L. Lions, *On the Schwarz alternating method. III: a variant for nonoverlapping subdomains*, in Third international symposium on domain decomposition methods for partial differential equations, vol. 6, SIAM Philadelphia, PA, 1990, pp. 202–223.

[18] P. Mamooler, *The Domain Decomposition Method of Bank and Jimack as an Optimized Schwarz method*, PhD thesis, University of Geneva, 2019.

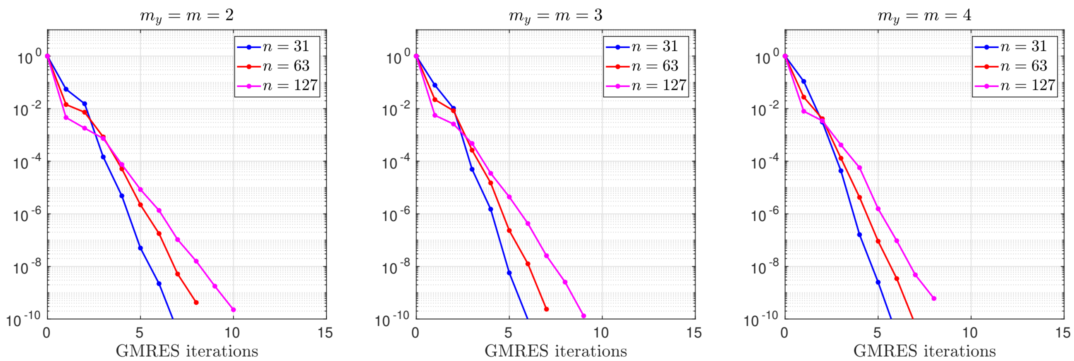

Fig. 4.14: Decay of the residual of the GMRES iteration preconditioned by BJM for $m_y = m = 2$ (left), $m_y = m = 3$ (middle) and $m_y = m = 4$ (right) uniformly distributed coarse points (in direction x and y) and overlap $L = 2h$.

[19] J. Mandel, *Balancing domain decomposition*, International Journal for Numerical Methods in Biomedical Engineering, 9 (1993), pp. 233–241.

[20] J. Mandel and M. Brezina, *Balancing domain decomposition for problems with large jumps in coeffic ients*, Mathematics of Computation of the American Mathematical Society, 65 (1996), pp. 1387–1401.

[21] H. A. Schwarz, *Über einen Grenzübergang durch alternierendes Verfahren. Vierteljahrsschrift der Naturforschenden Gesellschaft in Zürich*, vol. 15:272–286, 1870.

[22] A. St-Cyr, M. Gander, and S. Thomas, *Multiplicative, additive and restricted additive Schwarz preconditioning*, SIAM J. Sci. Comput., 29 (2007), pp. 2402–2425.

[23] A. St-Cyr, M. J. Gander, and S. J. Thomas, *Optimized restricted additive Schwarz methods*, in Domain Decomposition Methods in Science and Engineering XVI, O. B. Widlund and D. E. Keyes, eds., Berlin, Heidelberg, 2007, Springer Berlin Heidelberg, pp. 213–220.

[24] E. Süli, *An Introduction to the Numerical Analysis of Partial Differential Equations*, vol. February, Lecture notes, University of Oxford, 2005.

[25] A. Toselli and O. Widlund, *Domain decomposition methods-algorithms and theory*, vol. 34, Springer Science & Business Media, 2006.

MOX Technical Reports, last issues

Dipartimento di Matematica
Politecnico di Milano, Via Bonardi 9 - 20133 Milano (Italy)

51/2021 Ciaramella, G.; Kwok, F.; Mueller, G.
Nonlinear optimized Schwarz preconditioner for elliptic optimal control problems

52/2021 Ciaramella, G.; Mechelli, L.
An overlapping waveform-relaxation preconditioner for economic optimal control problems with state constraints

53/2021 Ciaramella, G.; Mechelli, L.
On the effect of boundary conditions on the scalability of Schwarz methods

50/2021 Ciaramella, G.; Vanzan, T.
On the asymptotic optimality of spectral coarse spaces

49/2021 Rea, F.; Savaré, L; Franchi, M.; Corrao, G; Mancia, G
Adherence to Treatment by Initial Antihypertensive Mono and Combination Therapies

50/2021 Rea, F.; Savaré, L; Franchi, M.; Corrao, G; Mancia, G
Adherence to Treatment by Initial Antihypertensive Mono and Combination Therapies

48/2021 Riccobelli, D.
Active elasticity drives the formation of periodic beading in damaged axons

47/2021 Orlando, G; Della Rocca, A; Barbante, P. F.; Bonaventura, L.; Parolini, N.
An efficient and accurate implicit DG solver for the incompressible Navier-Stokes equations

45/2021 Diquigiovanni, J.; Fontana, M.; Vantini, S.
Distribution-Free Prediction Bands for Multivariate Functional Time Series: an Application to the Italian Gas Market

46/2021 Diquigiovanni, J.; Fontana, M.; Vantini, F.
Conformal Prediction Bandsfor Multivariate Functional Data